Nanoscale

REVIEW

View Article Online
View Journal | View Issue

Cite this: *Nanoscale*, 2021, **13**, 12058

ZIF-67-based catalysts for oxygen evolution reaction

Hui Wen, †[a,b] Shengqi Zhang, †[a,b] Tao Yu,[a,b] Ziyu Yi[a,b] and Rui Guo *[a,c,b]

As a new type of crystalline porous material, the imidazole zeolite framework (ZIF) has attracted widespread attention due to its ultra-high surface area, large pore volume, and unique advantage of easy functionalization. Developing different methods to control the shape and composition of ZIF is very important for its practical application as catalyst. In recent years, nano-ZIF has been considered an electrode material with excellent oxygen evolution reaction (OER) performance, which provides a new way to research electrolyzed water. This review focuses on the morphological engineering of the original ZIF-67 and its derivatives (core–shell, hollow, and array structures) through doping (cation doping, anion doping, and co-doping), derivative composition engineering (metal oxide, phosphide, sulfide, selenide, and telluride), and the corresponding single-atom catalysis. Besides, combined with DFT calculations, it emphasizes the in-depth understanding of actual active sites and provides insights into the internal mechanism of enhancing the OER and proposes the challenges and prospects of ZIF-67 based electrocatalysts. We summarize the application of ZIF-67 and its derivatives in the OER for the first time, which has significantly guided research in this field.

Received 16th March 2021,
Accepted 14th June 2021

DOI: 10.1039/d1nr01669e

rsc.li/nanoscale

1 Introduction

The consumption of a large number of fossil fuels and the resulting greenhouse effect has prompted researchers to have a strong research interest in the development of clean energy conversion technologies.[1–5] In particular, the electrolysis of water to produce hydrogen is a convenient and environmentally friendly way to generate clean hydrogen energy.[6–9] However, the slow kinetics of anodic oxygen generation severely limits the hydrogen release reaction on the cathode.[10–12] Therefore, it is necessary to design electrocatalysts with a high-efficiency OER to improve the efficiency of water decomposition.[13–15] So far, IrO_2 and RuO_2 are catalysts with the highest OER activity in alkaline media.[16] However, both IrO_2 and RuO_2 are easily oxidized, and their high cost has seriously hindered the commercialization of zinc–air batteries and overall water splitting.[17–20] In recent years, researchers have done a lot of work to improve the performance of cheap electrocatalysts, hoping to replace precious metal-based catalysts.[21–23] Transition metal-based MOF derivatives are considered as promising alternative catalysts for the OER.[24] Researchers found that on this basis, the rational design and construction of the structure and composition of the catalyst can further improve the electrocatalytic performance of the OER.[25–27]

As a new type of crystalline and microporous material, the metal–organic framework (MOF), with a large surface area, unique porosity, and customizable functionality, is extremely attractive for catalysis.[28–30] Using active metal centers and functionalized organic ligands, MOFs combine the good properties of these two catalysts.[31,32] MOFs have broad prospects as OER electrode catalysts, because the pores and open channels of the MOF can provide storage space for the electrolyte, promote the diffusion of reactants, and promote the transport/release of generated oxygen. In addition, the evenly distributed metal cations in the MOF and the ligands in the framework are appropriately adjusted to effectively improve the ability of the OER catalyst.[33]

Although many types of MOF have been developed to catalyze the oxygen release reaction, most MOFs cannot be used in practical applications due to their poor stability. While, ZIF has excellent stability due to its special structure (the skeleton structure of ZIF-67 is composed of metal Co_2^+ ions and N atoms of 2-methylimidazole, which form tetrahedral structural units by hybridizing with the four-coordinate SOD topology). In addition, ZIF is a very attractive sub-category. It has the advantages of the large specific surface area of a MOF, high porosity, adjustable pore structure and the chemical and

[a]*School of Materials Science and Engineering, Northeastern University, Shenyang 110819, China. E-mail: guorui@neuq.edu.cn*
[b]*School of Resources and Materials, Northeastern University at Qinhuangdao, Qinhuangdao 066004, China*
[c]*Key Laboratory of Advanced Energy Materials Chemistry (Ministry of Education), College of Chemistry, Nankai University, Tianjin 300071, China*
† These authors contributed equally to this work.

thermal stability of traditional zeolite materials.[34–36] Although there have still been relatively few studies based on ZIF catalysts in recent years, they have shown a gradual growth trend.[37,38] Although ZIF-67 and its derivatives show excellent OER catalytic performance, there is still a gap in the practical application of overall hydrolysis. In addition, ZIF-8 is an indispensable isostructural MOF of ZIF-67, as many nanocatalysts utilize the structural difference/similarity of this pair of MOFs in constructing unique structures, but ZIF-8 is rarely used for OER catalysis.[39]

This review introduces the applications of ZIF-67 and its derivatives in catalytic regulation of the OER through two aspects: structural engineering and component engineering. In addition, by summarizing DFT calculations, we can give a deeper insight into its catalytic mechanism for the OER process, which provides a theoretical basis for more rational design of OER catalysts. Finally, the application prospects of ZIF-67 and its derivatives in OER catalysis are proposed.

2 Preparation and properties of ZIF-67

2.1 Preparation of ZIF-67

T-ZIF-67 is a commonly used catalyst in most studies of electrocatalytic OERs based on ZIF-67, while H-ZIF-67 and M-ZIF-67 are rarely used. Usually, the synthesis method of T-ZIF-67 (Fig. 1a) reported by Luo *et al.*[40] can be used as a reference to synthesize a purple product. Moreover, the synthesis of M-ZIF-67 (Fig. 1b) was carried out by only replacing $Co(NO_3)_2$ with $CoSO_4$ on the basis of the synthesis of T-ZIF-67; the synthesis of H-ZIF-67 (Fig. 1c) is based on the synthesis of M-ZIF-67 with PVP.

2.2 OER performance of ZIF-67

For the OER of ZIF-67, Wang *et al.*[41] proposed a new concept that could realize the engineering of the imidazole zeolite framework (ZIF-67) as a two-dimensional structure with exposed (002) faces in the MOF. They found that in the (002), (011), and (111) planes, the (002) plane of ZIF-67 showed the best OER activity (Fig. 2a and b). In contrast, it was found that ZIF-67 nanocrystals with a size comparable to the main exposed (011) plane had poor OER activity. Based on the experimental results and density functional theory (DFT) (Fig. 2c and d), they revealed the influence of the crystal face on the OER performance of ZIF-67.

In addition, Table 1 shows that, although pure ZIF-67 shows poor OER catalytic performance due to its low conductivity, it is very important to understand what is the real catalytically active site in the catalytic process. For example, Zheng *et al.*[42] used *in situ* spectroelectrochemical methods to prove that the true catalytically active sites in the catalytic process of ZIF-67 are α-$Co(OH)_2$ and CoOOH, not metal atom nodes. The changes to ZIF-67 during the catalytic process are shown in Fig. 2e.

In order to accurately show the OER performance of ZIF-67 derivatives, Schuhmann *et al.*[43] evaded the overall effect and film effect of the macroscopic analysis of the electrode reaction through an electrochemical study of single nanoparticles (Fig. 2f and g). Thus, the electrocatalytic performance of the OER and its catalytic process can be measured more accurately. According to reports, this unprecedented method can be used to understand the electrocatalytic behavior of individual nanoparticles without affecting the overall and thin-film effects. This research program consolidates the potential of such architectures to establish the basic electrocatalytic parameters of nanoparticles and structure–property relationships that are not affected by macroscopic membrane effects. In addition to obtaining the basic electrocatalytic properties of nanoparticles, these nanocomponents can also be used as a powerful platform for studying reactions involving changes in the local electrode–electrolyte environment, which is not possible on large electrodes. Subsequently, the group[44] reported studies of Co–N-doped C composite particles derived from the ZIF-67 relative to the OER using a scanning electrochemical cell microscope (SECCM) (Fig. 2h). By using the interference-free Os compound as a standard for the free-diffusion internal redox potential, the problem of surface wetting and potential drift can be solved, and SECCM can be successfully applied in alkaline media.

2.3 Summary

This section mainly introduces three types of ZIF-67 (T-ZIF-67, M-ZIF-67, H-ZIF-67) for the electrocatalytic OER. Among them, T-ZIF-67 is the most commonly used, and an efficient OER is achieved by shaping the zeolite imidazolate skeleton (ZIF-67) into a 2D structure with exposed (002) facets. It can be found that the real active sites of ZIF-67 are α-$Co(OH)_2$ and CoOOH.

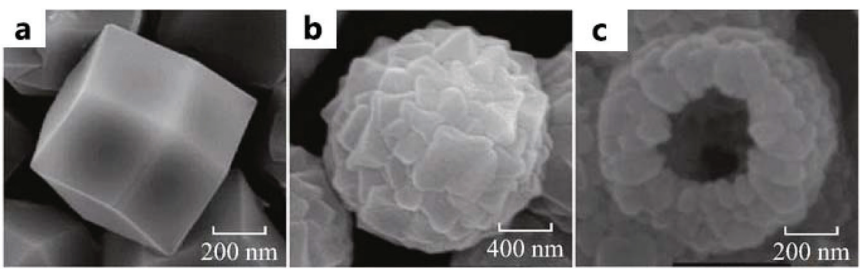

Fig. 1 SEM images of (a) T-ZIF-67, (b) M-ZIF-67, and (c) H-ZIF-67.[40] Copyright @2017, The Author(s).

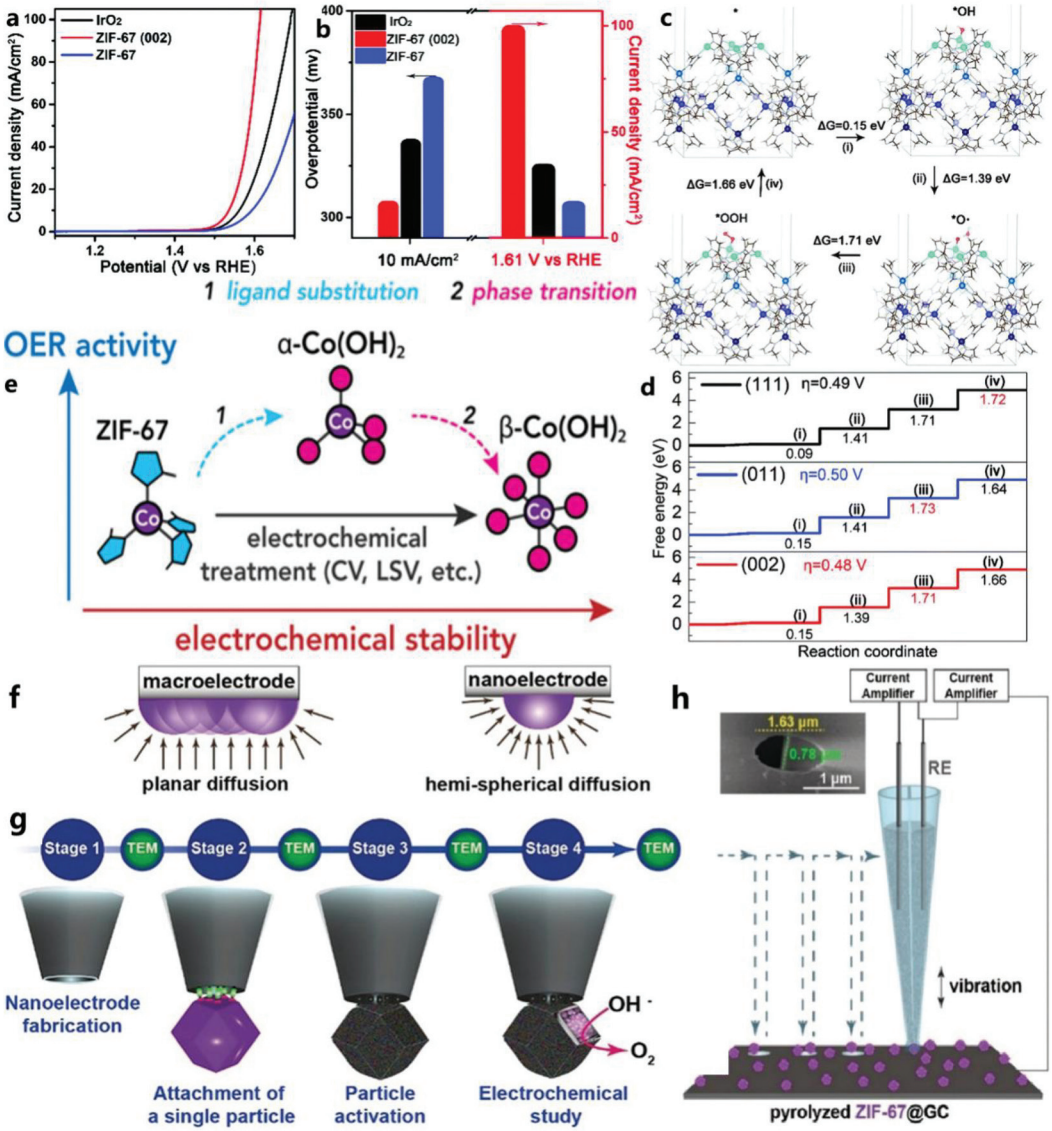

Fig. 2 (a) Linear sweep voltammetry plots of commercial IrO_2, ZIF-67 (002) and ZIF-67, (b) and the overpotential and current density of the corresponding catalysts at 10 mA cm^{-2}. (c) The surface energy level of the OER process of ZIF-67 (002). Metal Co is blue, O is red, and H is white. (d) The standard free energy step diagram of the OER process on the (002), (011), and (111) planes of ZIF-67.[41] Copyright © 2020, Royal Society of Chemistry. (e) Structure and morphological evolution of MOF (zeolite imidazolate skeleton ZIF-67) determined by cyclic voltammetry and amperometric methods.[42] Copyright © 2020, American Chemical Society. (f) Illustration of diffusion flux around a macroelectrode and a nanoelectrode. (g) Flowchart of the various stages involved in the study of the MOF-derived CoN/C nanoparticle.[43] Copyright © 2019 Wiley-VCH Verlag GmbH & Co. KGaA, Weinheim. (h) Typical SECCM setup and SEM image of the double-barrel nanocapillary used as the SECCM tip (inset).[44] Copyright © 2019 The Authors. Published by Wiley-VCH Verlag GmbH & Co. KGaA.

In addition, the OER catalytic process of ZIF-67 derivatives and the study of its single nanoparticle electrocatalytic behavior are also described.

3 OER catalysis of ZIF-67 with different morphological structures

As we all know, improving the electrocatalytic performance through composition optimization and morphological modification are two effective and feasible methods. In addition, the conductivity and stability of MOF and MOF-derived catalysts are issues of great concern, and these problems can be solved to a certain extent through composition or morphology engineering. It can be found that the main purpose of structural or morphological engineering is to expand the active surface area to expose more active sites. For example, the controlled synthesis of a core–shell structure, a hollow structure and an array can result in an excellent OER performance. The morphological engineering of MOF and MOF derivatives is very important

Table 1 The catalytic performance of ZIF-67 reported in the literature

Catalyst	Substrate	Overpotential/mV	Tafel/mV dec^{-1}	Electrolyte	Scan rate/mV s^{-1}	Ref.
ZIF-67	RDE	334	105	1 M KOH	5	45
ZIF-67	Glassy carbon electrode (GCE)	400	235	1 M KOH	5	46
ZIF-67	Glassy carbon electrode (GCE)	420	—	1 M KOH	1	47
ZIF-67	RDE	400	96	1 M KOH	5	48
ZIF-67	Glassy carbon electrode (GCE)	390	88.3	1 M KOH	5	49
ZIF-67	Glassy carbon electrode (GCE)	352	82	1 M KOH	5	50
ZIF-67	Glassy carbon electrode (GCE)	410	83.8	1 M KOH	2	51
ZIF-67	Glassy carbon electrode (GCE)	408	128.2	1 M KOH	5	52
ZIF-67	Glassy carbon electrode (GCE)	530	147	1 M KOH	2	53
ZIF-67	NF	400	98	1 M KOH	5	54
ZIF-67	Glassy carbon electrode (GCE)	530	125.5	0.1 M KOH	5	55
ZIF-67	Glassy carbon electrode (GCE)	546	74	1 M KOH	5	56
ZIF-67	Glassy carbon electrode (GCE)	480	122	0.1 M KOH	5	57

to increase the density of active sites, control the uniform distribution of active materials, prevent nanoparticle aggregation, promote electron/mass transfer, and produce synergistic effects between active materials and the matrix.[58] However, the low intrinsic conductivity and easy self-aggregation of ZIF-67 derivatives usually result in high overpotentials. The result is insufficient exposure of ZIF-67 surface active sites and slow interfacial reaction kinetics. A single derivative of ZIF-67 usually exhibits an unsatisfactory electrochemical performance.[59] Therefore, it is necessary to optimize the morphology to improve the catalytic performance of ZIF-67 and its derivatives.

3.1 Core–shell structure

Traditional catalytic reactions mostly occur on the surface of the solid phase, so the total surface area of the active phase has a great influence on the reaction rate. This also shows that the surface structure will affect the catalytic activity and its selectivity, and appropriately increasing the specific surface area can increase the catalytic activity. The study found that the catalyst with a core–shell structure could maintain the catalytic activity well.[60–62] The structure of the catalyst has the advantages of large specific surface area and large pore size, which can solve the problem of nanomaterials easily agglomerating. Furthermore, because the boundary between the core and the shell is more obvious, the reaction ratio is more independent, there are more catalytically active sites, and the coating between materials maximizes the synergistic catalysis effect.[63]

3.1.1 Single shell structure (S-SS). Adjusting the shell can improve the oxygen evolution performance of the catalyst with ZIF-67 or its derivatives as the core has become a research hotspot. For example, Chai *et al.*[64] prepared a ZIF-67@$Co(OH)_2$ core–shell nanostructured catalyst (Fig. 3a and b). The core and shell synergy in ZIF-67@$Co(OH)_2$ can improve the charge transfer rate and the reaction kinetics for the OER.

In addition, ZIF-67 or its derivatives can also be used as a shell for the catalyst. This not only increases the specific surface area but also protects the active sites of the reaction and increases its electrical conductivity. For example, Hou *et al.*[65] used a new gas-phase hydrothermal method to synthesize ultra-thin cobalt-based ZIF-67 nanosheets on a vertically arranged $Co(OH)_2$ nanosheet array. Ultra-thin ZIF-67 nanosheets are grown on the surface of $Co(OH)_2$ sheets (with a thickness of about 5 nm), forming a core–shell structure (Fig. 3c). The excellent OER performance of this catalyst is due to inherent excellent electrical conductivity of exfoliated graphene foil and the synergistic effect between $Co(OH)_2$ and the ZIF-67 interface, thereby accelerating the charge transfer and mass transfer process. Carbon material with excellent conductivity is another material to be used as a shell to improve the conductivity of the catalyst to endow the catalyst with an excellent OER performance. For example, Zheng *et al.*[66] chose cobalt-based ZIF-67 as the precursor of cobalt and carbon, and then converted them into $Co_{0.85}Se$ nanoparticles (called ZIF-$Co_{0.85}Se$) through selenization and subsequent calcination (Fig. 3d). As-prepared ZIF-$Co_{0.85}Se$ has an ultra-thin carbon shell layer (Fig. 3e and f), which is beneficial for improved conductivity and catalytic activity of the catalyst. The Co^{3+}- and carbon-rich layer structure can provide sufficient active centers, good electrical conductivity and effective charge transport during the catalytic process, so as to achieve excellent OER catalytic performance. Meanwhile, they found that organic compounds as the core–shell structure could also effectively improve the specific surface area of the catalyst. For instance, Qin *et al.*[67] described hybrid electrocatalysts with strongly coupled metal (Co–Fe) polyphenol networks (MPNs) and Fe_3O_4 nanoparticles (Fig. 3g). These catalysts were prepared through tannic acid-mediated conversion of the surface layer of ZIF-67@Fe_3O_4 synthesized initially during the selective conversion process, so that the core–shell nanoparticles were uniformly covered by the organic MPN layer. The MPN layer is composed of metal phenolic compounds rich in molecular metal hydroxide (M–OH, M–O–M) centers, which increase the electrochemical surface area by about four times. Pang *et al.*[46] grew π-conjugated organic molecules *in situ* on ZIF-67 (HHTP@ZIF-67) by the hot solvent method (Fig. 3h). HHTP@ZIF-67 has a large specific surface area (Fig. 3i), leading to a great improvement in the OER catalytic performance.

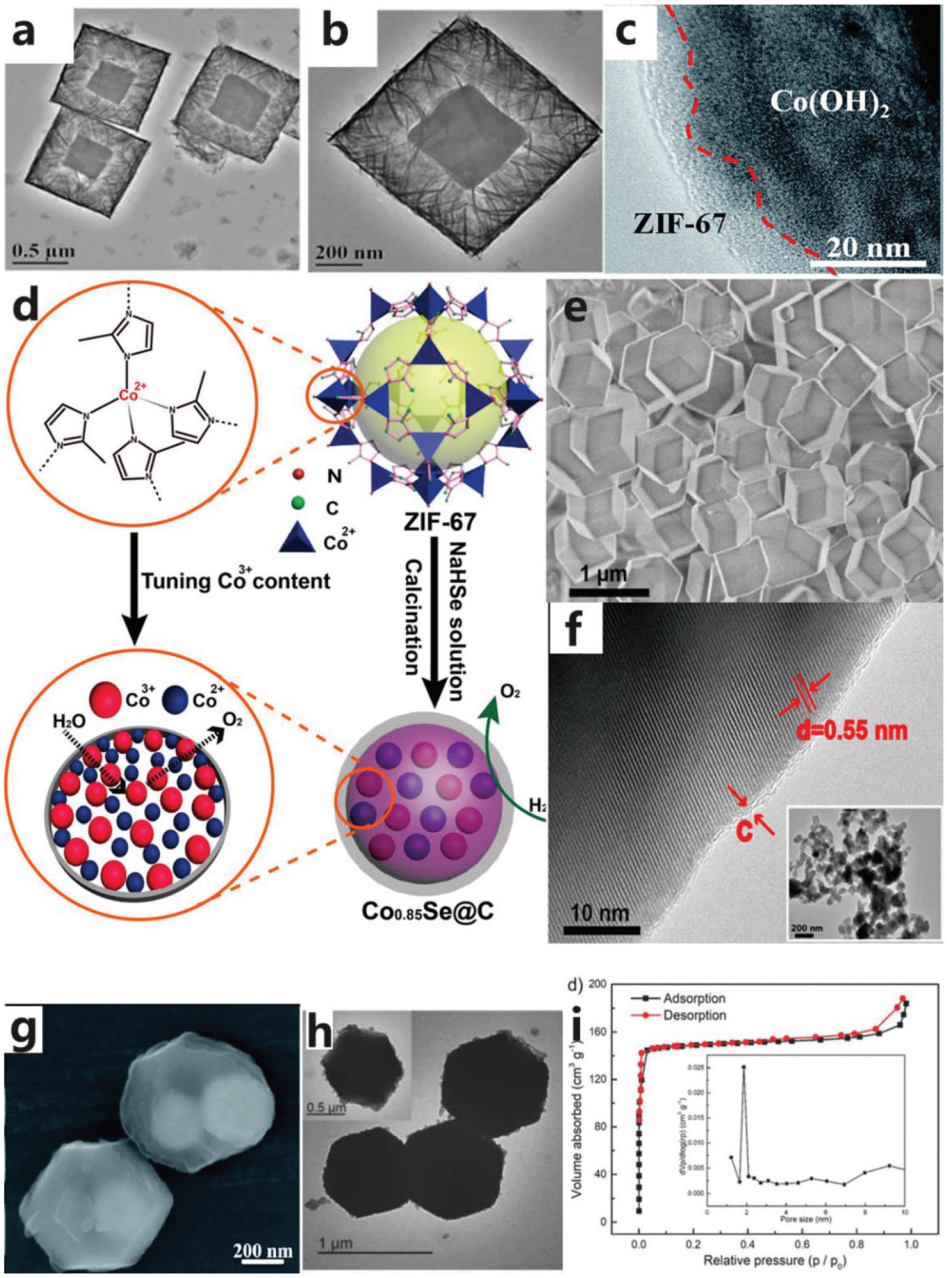

Fig. 3 (a and b) TEM images of $Co(OH)_2$-1.[64] Copyright © 2019 Elsevier Inc. All rights reserved. (c) HRTEM images of the EG/$Co(OH)_2$/ZIF-67 hybrid.[65] Copyright © 2018, Royal Society of Chemistry. (d) Schematic diagram of the synthesis of $Co_{0.85}Se$@C nanoparticles. (e) SEM image of ZIF-67. (f) HRTEM image of ZIF-$Co_{0.85}Se$. Inset: low-resolution TEM image.[66] Copyright © 2016, American Chemical Society. (g) SEM images of ZIF-67@Fe_3O_4 nanoparticles.[67] Copyright © 2019, Royal Society of Chemistry. (h) TEM images of HHTP@ZIF-67. (i) The Brunauer–Emmett–Teller (BET) specific surface area and the corresponding pore size distribution plot (inset) of HHTP@ZIF-67.[46] Copyright © 2018 Wiley-VCH Verlag GmbH & Co. KGaA, Weinheim.

3.1.2 Double shell structure (D-SS). The biggest advantage of the D-SS is to increase the specific surface area of the catalyst by introducing a gap between the core and the shell, thereby exposing more active sites, so it has a better OER catalytic performance. For example, Zou and others[68] successfully synthesized Co_3O_4@Z67-NT@CeO_2 through hydrothermal and high-temperature pyrolysis methods, which could maintain the original morphology of the ZIF-67 polyhedron (Fig. 4a and b). The porous D-SS of Co_3O_4@Z67-700@CeO_2 also promotes complete contact between the CeO_2/Co_3O_4 interface and the surface, which exposes more active sites to promote the OER. Pang *et al.*[69] successfully synthesized the ZIF-8@ZIF-67@POM catalyst by using a simple co-precipitation method (Fig. 4c and d). Due to the synergy between POM and ZIF substances, the regular structure and high surface area, the prepared ZIF-8@ZIF-67@POM catalyst has an excellent OER electro-

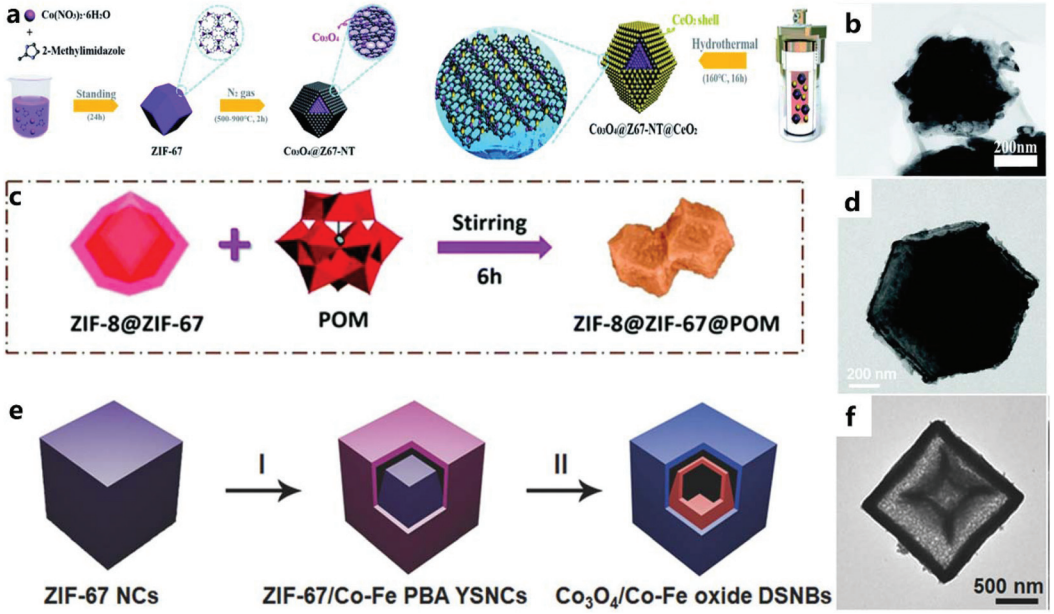

Fig. 4 (a) Synthesis route for the Co_3O_4@Z67-NT@CeO_2 composites. (b) TEM images of Co_3O_4@Z67-N700@CeO_2.[68] Copyright © 2019, Royal Society of Chemistry. (c) Schematic diagram for the synthesis of ZIF-8@ZIF-67@POM. (d) TEM image of ZIF-8@ZIF-67@POM.[69] Copyright © 2019, Royal Society of Chemistry. (e) Schematic illustration of the formation process of Co_3O_4/Co–Fe oxide DSNBs. (f) TEM images of Co_3O_4/Co–Fe oxide DSNBs.[70] Copyright © 2018 Wiley-VCH Verlag GmbH & Co. KGaA, Weinheim.

catalytic performance. Compared with the hydrothermal method, this co-precipitation method is simpler and more convenient and does not require a high-temperature environment. The ion exchange reaction is very beneficial for the structure and chemical composition of complex MOF-derived nanomaterials. Therefore, Lou *et al.*[70] prepared a Co_3O_4/Co–Fe oxide double-shell nanobox catalyst through an anion exchange and annealing process (Fig. 4e and f). Due to the advantages of structure and composition, the catalyst exhibits an excellent OER electrocatalytic performance.

3.1.3 Egg yolk/core–shell structure (E/CS). In addition to the S-SS and D-SS, the E/CS can also effectively promote the catalytic reaction of oxygen evolution.[71] Direct synthesis and pyrolysis are the two commonly used methods. Compared with the S-SS, the E/CS has a larger specific surface area and has a more stable structure than the D-SS. For example, Pang *et al.*[72] successfully synthesized an egg yolk/egg shell ZIF-67@POM catalyst (Keggin type polyoxometalate (POM)) (Fig. 5a and b). This unique structure has a synergistic effect between the POM and ZIF-67, which can effectively improve the catalytic performance of the catalyst (Fig. 5c), and the catalyst has intentional cycling stability and a high specific surface area. Li *et al.*[73] used ZIF-67 as the precursor to prepare hollow N-doped carbon polyhedral Co-based nanoparticles through a two-step pyrolysis-oxidation method (Fig. 5d). The main point of this synthesis method is to accurately and effectively control the oxidation process of Co NPs, so that a series of Co–Co_3O_4 nanostructures embedded in hollow nitrogen-doped carbon polyhedra (HNCP) (core–shell Co/Co_3O_4, egg yolk@shell Co@Co_3O_4, and hollow Co_3O_4 weeks NP) can be prepared. The best Co_3O_4/HNCP-40 (Fig. 5e–j) material has an extremely high OER activity and a small overpotential of 333 mV when it reaches a current density of 10 mA cm^{-2}, which is one of the highest performing OERs reported based on a Co catalyst (Fig. 5k and l).

3.1.4 Summary. In summary, nano-core–shell OER catalysis can achieve effective catalytic performance due to the specific surface nanostructure, porosity, and the synergy between the shell and the core. Among them, the core/shell structured catalyst not only realizes a controllable catalytic reaction, but can also protect the core material from chemical attack by the external environment, and solve the agglomeration problem of nanoparticles. In recent years, it has become a research focus in the field of catalysis. However, the instability of the core–shell structure will cause the active surface area and catalytic performance to rapidly decrease over time, which severely limits the widespread use of core–shell structured catalysts in the industrial field. Besides, we summarized the OER catalytic performance based on the ZIF-67 core–shell structure for comparison (Table 2 and Fig. 6), and found that the shell structured catalyst had an excellent OER catalytic performance. It can be seen that the performance of the catalyst with a core–shell structure has been significantly improved after carbonization (most of which are concentrated in Tafel (55–80 mV dec^{-1}) and overpotential (250–350 mV)). In addition, it can be seen that different treatment methods also seriously affect the catalyst.

3.2 Hollow structure (HS)

Hollow catalysts have been widely used in the electrolysis of water to produce oxygen due to their unique structural characteristics. The high surface area and thin shell give a HS catalyst

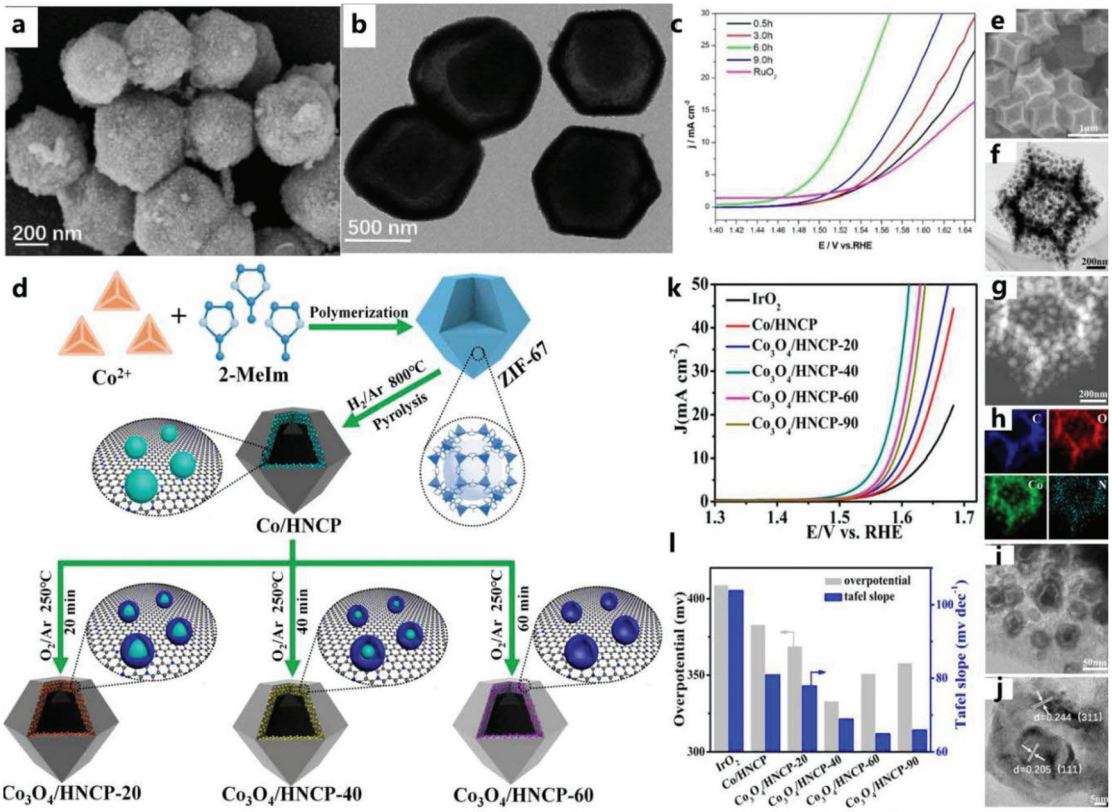

Fig. 5 (a) SEM and (b) TEM images of 6-ZIF-67@POM. (c) The OER polarization curve of the catalyst in 1 M KOH solution at a scan rate of 2 mV s^{-1}.[72] Copyright @ 2019, American Chemical Society. (d) Schematic diagram of the synthesis of a series of Co–Co_3O_4 based nanostructures embedded in a hollow nitrogen-doped carbon polyhedron. (e–j) SEM, TEM, STEM, EDS mapping, and HRTEM images of Co_3O_4/HNCP-40, (k) LSV curves, (l) plot summarizing Tafel results and overpotentials at j = 10 mA cm^{-2}.[73] Copyright @ 2018, American Chemical Society.

abundant surface active sites and a high diffusion efficiency.[86–88] As described by Lee *et al.*[89] the HS has huge cavities and porous thin walls, which promote the diffusion of electrolytes and ions, expose more electrochemically active sites, and reduce the electron transfer resistance. The hollow and porous structure provides the catalyst with a large specific surface area and high porosity, which can expose more electrocatalytically active sites during the catalytic process to improve the catalytic activity. In addition, this structure can also increase the conduction and diffusion of electrons through the four-electron pathway to create multiple available channels to promote electrocatalytic activity. This simple method for preparing porous hollow metal oxide electrode materials based on MOF templates can provide new ideas for the low-cost, environmentally friendly, and efficient development of hollow-structured catalysts.

3.2.1 Pyrolysis method. The HS can be synthesized simply by controlling the sintering temperature, time, and some related auxiliary conditions. For example, Li *et al.*[56] prepared regular porous hollow polyhedral cobalt oxide (Co_3O_4 hollow polyhedron) by the one-step pyrolysis of ZIF-67 (Fig. 7a). Compared with granular Co_3O_4 (Co_3O_4 particles), Co_3O_4 hollow polyhedra show excellent OER activity (Fig. 7b). Although this method is simple and convenient to operate, the catalytic performance is not ideal. Men *et al.*[90] synthesized the h-Co_3O_4@rGO catalyst through a two-step annealing process (Fig. 7c and d). Co_3O_4 is encapsulated by GO to endow the catalyst with good conductivity, a high surface area and unique hollow morphology. After one annealing treatment, the synthesized h-Co_3O_4@rGO composite shows a better performance than Co_3O_4-rGO (Fig. 7e). In order to further optimize the pyrolysis method, Liang *et al.*[91] first reported a simple KCl-assisted pyrolysis method, using ZIF-67 as a precursor, and embedding Co nanoparticles into N-doped carbon nanotube hollow polyhedra (NCNHP) to construct a hybrid architecture (Fig. 7f and g). During pyrolysis in an environment of 400 °C, potassium chloride will accelerate the decomposition of ZIF-67 and promote the formation of carbon nanotubes (CNT) *in situ*. Due to the synergy between Co nanoparticles and N-doped CNTs and the unique layered structure, NCNHP exhibits an excellent OER catalytic performance.

3.2.2 Template method. The use of the template method to fine-tune the pre-synthesized template to generate the HS is a promising preparation method. For example, Li *et al.*.[92] introduced a continuous self-sacrificing template strategy in which ZIF-67@NiCo-LDH CS was dispersed in ethanol and water to remove the ZIF-67 template and obtain $NiCo_2O_4$/Co, N-CNTs NCs (Fig. 8a). In addition, it can be found that the reflux

Table 2 Comparison of different core–shell catalysts based on ZIF-67 and its derivatives

Core–shell structure	Substrate	Electrolyte	Overpotential/ mV	Tafel/mV dec^{-1}	BET (m^2 g^{-1})/BJH	Current density/mA cm^{-2}	Ref.
Co_3O_4@Z67-N700@CeO_2	GCE	2–0.1 M KOH	350	80.7	267.27/micropores	10	68
Co-NC@CoP-NC	GCE	0.1 M KOH	330	79	243/micropores	10	74
Co@Co_3O_4	RDE	0.1 M KOH	410	54.3	76	10	75
Co@Ir/NC-10%	RRDE	1 M KOH	280	73.8	108.45/micropores	10	76
ZIF-67@POM	GCE	1 M KOH	287	58	116/micropores	10	72
ZIF-8@ZIF-67@POM	GCE	2–1 M KOH	480	88	340/mesopores	10	69
CoP/CN@MoS_2	(GC) RDE	1 M KOH	289	69	—	10	77
NiCoP/C@FeOOH	GCE	1 M KOH	271	69	—	10	78
Co-BO@Co_3O_4	GCE	1 M KOH	342	32.7	55.08/macropores	10	79
Co_3O_4/Co–Fe	GC–RDE	1 M KOH	297	61	43.3/micropores/ mesopores	10	70
HHTP@ZIF-67	GCE	1 M KOH	238	104	2013.9/mesopores	10	46
ZIF-$Co_{0.85}$ Se@C	GC–RDE	1 M KOH	360	62	13.56	10	66
Co_3O_4/HNCP-40	GCE	1 M KOH	333	69	204/micropores/ mesopores	10	73
ZIF-67@$Co(OH)_2$	GCE	1 M KOH	354	73.3	—	10	64
EG/$Co(OH)_2$/ZIF-67	EG	1 M KOH	280	63	—	10	65
MPN@Fe_3O_4	GCE	1 M KOH	260	33.6	8.7/macropores	10	67
N-GC/Co@CoO/rGO	GCE	1 M KOH	360	—	516/micropores	10	80
FCNC900	GCE	1 M KOH	360	90	217/micropores	10	81
CoP/NCNHP	GCE	1 M KOH	320	70	86.5/micropores/ mesopores	10	82
Co_9S_8@Co_9S_8@MoS_2-0.5	GCE	1 M KOH	340	82.7	42.14	10	83
$Co(S_{0.46}Se_{0.54})_2$@C	GCE	0.1 M KOH	220	56.8	46.9/mesopores	10	84
CoP@FeCoP/NC YSMPs	CP	1 M KOH	238	47.98	24.85/mesopores	10	85

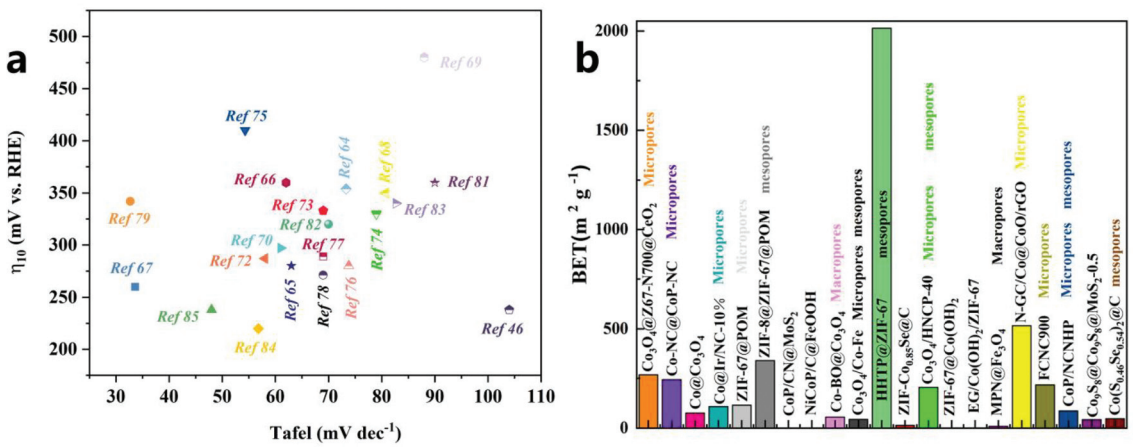

Fig. 6 (a) OER activity comparison graph showing the Tafel slope at an overpotential of 10 mA cm^{-2} for different catalysts. (b) Comparison of BET/BJH results for different catalysts.

process is widely used in the template method. For example, Xu *et al.*[47] uniformly dispersed ZIF-67 particles in an ethanol solution of thioacetamide, and then prepared amorphous CoS hollow nanocages (Fig. 8b) under reflux conditions at high temperature. Based on randomly broken particles, their thickness is estimated to be about 20 nm. Precise control of the reaction time between thioacetamide (TAA) and ZIF-67 NC can lead to the formation of hollow CoS_2 nanostructures. Finally, the catalyst CeO_x/CoS was obtained through a series of preparations, and this catalyst showed excellent OER catalytic performance (Fig. 8c).

Lyu and others[93] prepared a CoO–MoO_2 nanocage catalyst with excellent OER performance by refluxing the template (Fig. 8d and e). The $CoMoO_4$–$Co(OH)_2$ nanocage was prepared by the dissolution–regeneration method. The dissolution part involves etching ZIF-67 in the presence of water to release Co_2^+ ions. Na_2MoO_4 and Na_2WO_4 destroy the nanocage structure because dissolution is faster and regeneration is slower.

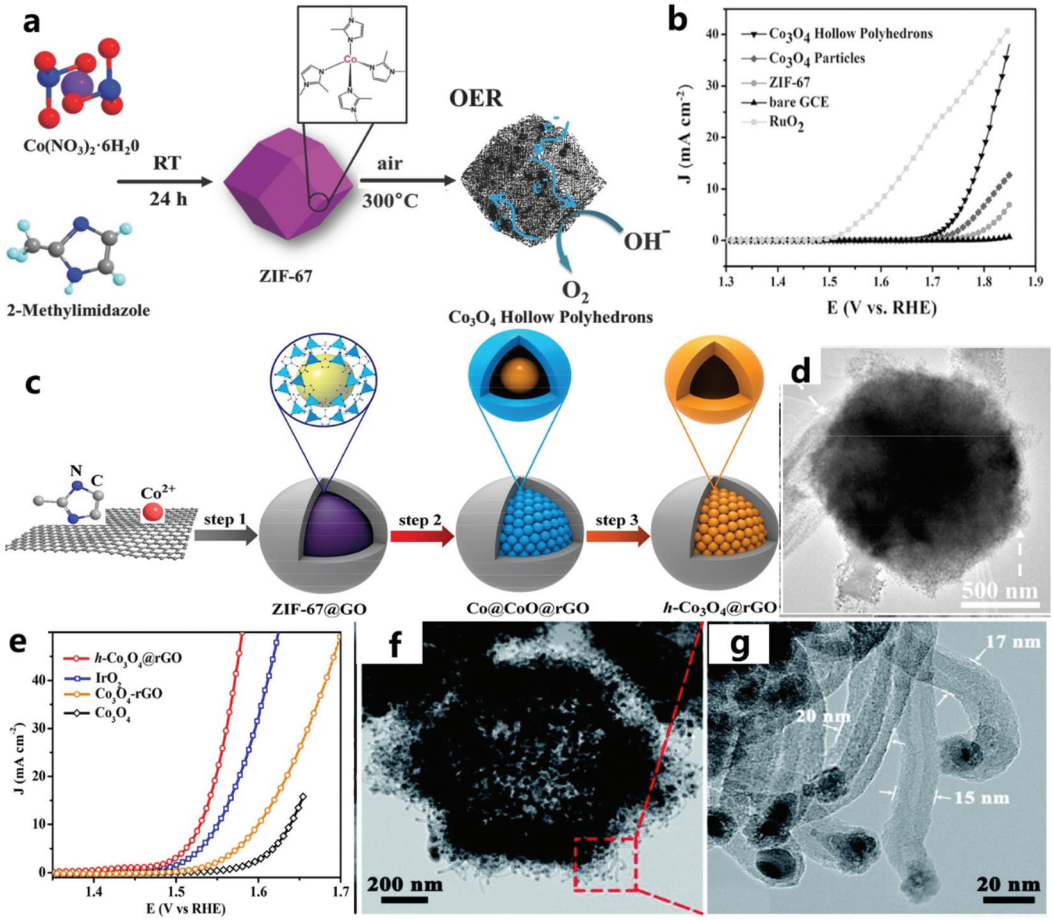

Fig. 7 (a) Schematic diagram to illustrate the OER electrocatalytic principles of Co_3O_4 hollow polyhedra. (b) The polarization curve of the catalyst in 1 M KOH solution at a scanning speed of 2 mV s^{-1}.[56] Copyright © 2016 Wiley-VCH Verlag GmbH & Co. KGaA, Weinheim. (c) Schematic diagram of the preparation of the h-Co_3O_4@rGO hollow catalyst using ZIF-67@GO as a precursor. (d) TEM image of h-Co_3O_4@rGO. (e) The LSV curve of the catalyst at a scanning speed of 1 mV s^{-1}.[90] Copyright @ 2018, American Chemical Society. (f) TEM image of NCNHP-1-500. (g) CNTs in an enlarged TEM image of NCNHP-1-500.[91] Copyright © 2019, Royal Society of Chemistry.

However, in addition to providing an alkaline environment for the formation of $Co(OH)_2$, Na_2MoO_4 can also provide MoO_4^{2-}. Appropriate regeneration and dissolution rates can maintain the nanocage structure. As the reaction continues, the outward diffusion of Co_2^+ results in the formation of voids in $CoMoO_4$–$Co(OH)_2$. With the dissolution of the ZIF-67 core, a hollow $CoMoO_4$–$Co(OH)_2$ nanocage is finally formed, and the $CoMoO_4$–$Co(OH)_2$ nanocage is reduced to CoO–MoO_2 during subsequent calcination under a reducing atmosphere.

3.2.3 Ion exchange method. When elements such as oxygen, sulfur, phosphorus, and selenium react with the metal surface, they become anions and occupy a larger space, which will cause them to move slowly in the metal nanostructure. In addition, to satisfy the driving force for the movement of the atoms, metal atoms that are small relative to the anion must diffuse outward. Therefore, the metal ions diffuse to the surface faster and react with anions on the surface, which causes the metal template of the core to be consumed, thereby forming the so-called Kirkendall cavity.[94] During the reaction process, the experimental conditions can be adjusted to synthesize the required hollow nanostructures.[95]

For example, Li *et al.*[96] used a convenient ion exchange method (*i.e.*, an anion exchange reaction between the ZIF-67 crystal and Ni^{2+}) to carefully synthesize a hollow (Co, Ni)Se_2 nanocage from ZIF-67. More specifically, the formation of the nanocage involves a dissolution–regeneration process, and the entire diffusion process can be attributed to the Kirkendall effect.

3.2.4 Summary. In summary, this section describes the preparation of HSs for OER catalysis by different methods (pyrolysis method, template method, and ion exchange method) and compares the OER catalytic performance of the HS prepared from ZIF-67 (Fig. 9 and Table 3). It can be found that the performance of most catalysts fluctuates within a certain range of values. Some catalysts have better catalytic performance due to the doping of iron and the etching of the hollow structure. In addition, we can find that the specific surface area and porosity of the catalyst can be effectively con-

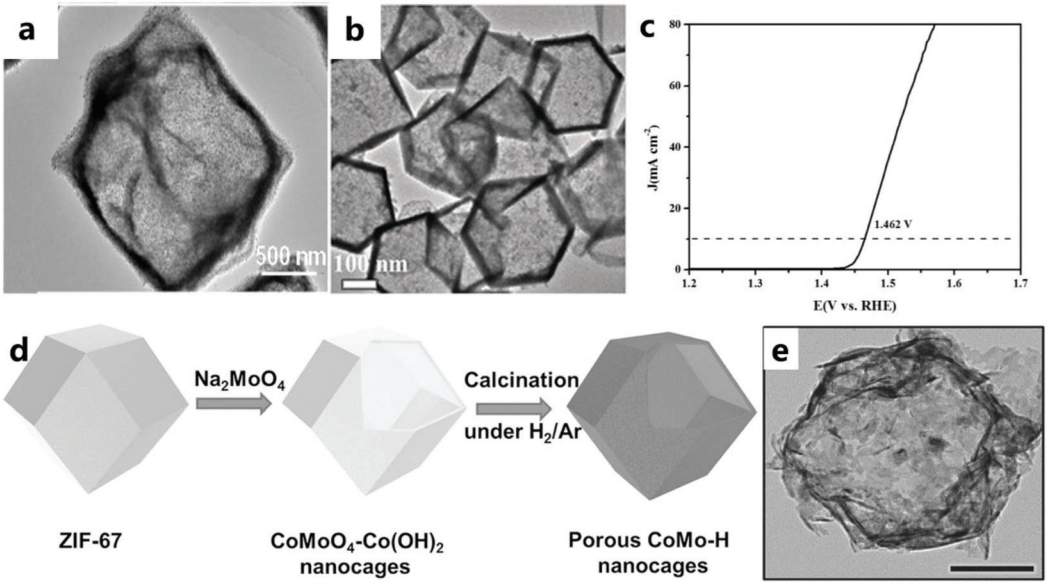

Fig. 8 (a) TEM image of $NiCo_2O_4$/Co, N-CNTs NCs.[92] Copyright @ 2018, American Chemical Society. (b) TEM image of precursor CoS. (c) LSV curve of CeO_x/CoS/CC catalyst for the OER.[47] Copyright © 2018 Wiley-VCH Verlag GmbH & Co. KGaA, Weinheim. (d) Schematic illustration describing the formation process of CoO–MoO_2 nanocages. (e) TEM image of CoMo–H.[93] Copyright © 2017 Wiley-VCH Verlag GmbH & Co. KGaA, Weinheim.

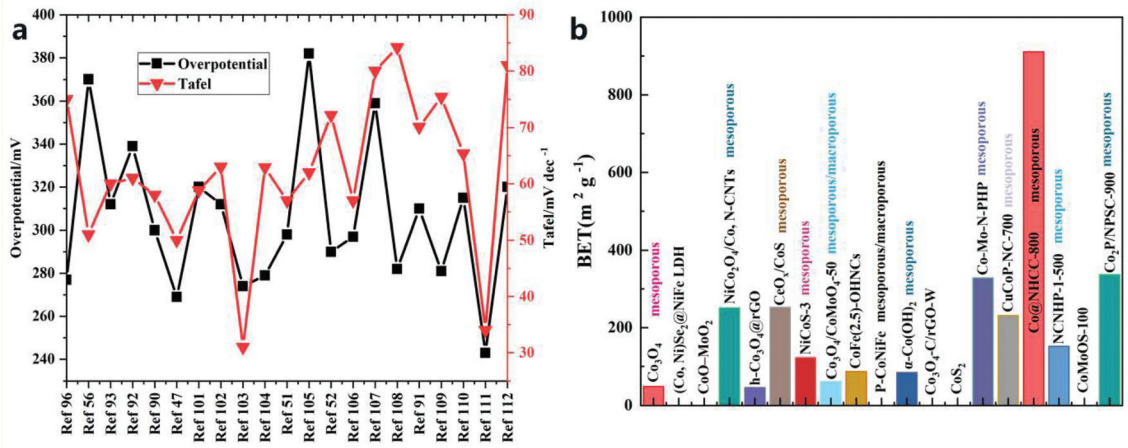

Fig. 9 Comparison of (a) Tafel slope and overpotential at a current density of 10 mA cm^{-2} and (b) BET/BJH results for different catalysts.

trolled through different synthesis methods. Some recent studies have found that the concave surface of the hollow nanostructure has a higher electrocatalytic activity than the convex surface.[97,98] In addition, due to the dissolution of core components, hollow nanoparticles tend to form disturbances or defects in their structures, which will increase the catalytic surface area.[99,100] Therefore, the preparation of hollow nanostructured catalysts with a controllable surface will be the goal of our research in this area.

3.3 Array

The reasonable design of a nanoarray structure grown *in situ* can effectively improve the OER performance.[113,114] In addition, catalysts using ZIF-67 arrays show excellent catalytic performance, but there are few studies in this field.

As far as the OER based on the ZIF-67 framework is concerned, Jiang *et al.*[115] chose nickel foam as the substrate for preparing CoO arrays (Fig. 10a and b). The CoO nanowire array is grown vertically on Ni foam and then selected as the precursor to provide the framework for the growth of Co_2^+ ions and ZIF-67 and dissolve its ligands with the help of a solvent. In addition, ZIF-67 nanorod arrays were successfully grown on Cu mesh, Fe mesh, and Cu foil by following similar synthesis steps. All these results demonstrate the universality of the current synthesis strategy for MOF-based hybrid arrays. The excellent electrocatalytic performance can be attributed to the more rapid release of air bubbles from the exposed active sites

Table 3 Comparison of different hollow catalysts based on ZIF-67 and its derivatives

HS	Substrate	Electrolyte	Overpotential/mV	Tafel/mV dec^{-1}	BET (m^2 g^{-1})/BJH	Current density/mA cm^{-2}	Ref.
(Co, Ni) Se_2@NiFe LDH	GC-RDE	1 M KOH	277	75	—	10	96
Co_3O_4	GCE	1 M KOH	370	51	49.27/mesoporous	10	56
CoO–MoO_2	GCE	1 M KOH	312	60	—	10	93
$NiCo_2O_4$/Co, N-CNTs	GCE	0.1 M KOH	339	61	251/mesoporous	10	92
h-Co_3O_4@rGO	GCE	1 M KOH	300	58	46.5	10	90
CeO_x/CoS	GCE	1 M KOH	269	50	252.92/mesoporous	10	47
NiCoS-3	GCE	1 M KOH	320	58.8	123/mesoporous	10	101
Co_3O_4/$CoMoO_4$-50	GC-RDE	1 M KOH	312	63	61.3/mesoporous/macroporous	10	102
CoFe(2.5)-OHNCs	GCE	1 M KOH	274	31	86.9	10	103
P-CoNiFe	GCE	1 M KOH	279	62.9	Mesoporous/macroporous	10	104
α-$Co(OH)_2$	GCE	1 M KOH	298	57	84.7/mesoporous	10	51
Co_3O_4–C/rGO-W	GCD	0.1 M KOH	382	62	—	10	105
CoS_2	GCE	1 M KOH	290	72.2	—	10	52
Co–Mo–N–PHP	GC-RDE	1 M KOH	297	57	328.5/mesoporous	10	106
CuCoP-NC-700	GCE	1 M KOH	359	80	232/mesoporous	10	107
Co@NHCC-800	GCE	1 M KOH	282	84.2	910.71/mesoporous	10	108
NCNHP-1-500	GC-RDE	1 M KOH	310	70.1	152/mesoporous	10	91
CoMoOS-100	GCE	1 M KOH	281	75.4	—	10	109
Co_2P/NPSC-900	Carbon paper	1 M KOH	315	65.36	337.215/mesopores	10	110
ZIF-67@CoFe-PBA-F	GC	1 M KOH	243	34	—	10	111
CoFe–Co@PNC-12	GC	0.1 M KOH	320	81	564/micropores	10	112

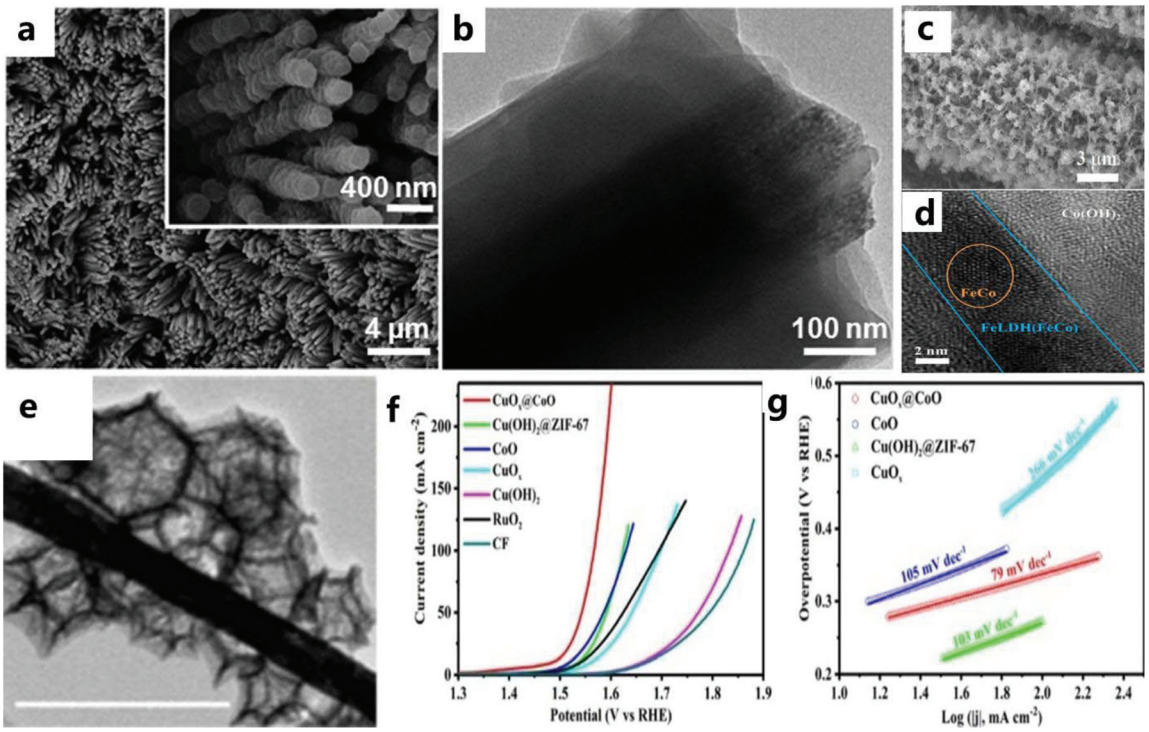

Fig. 10 (a) SEM and (b) TEM images of as-prepared Ni@CoO@ZIF-67 arrays. Inset: enlarged SEM image.[115] Copyright © 2017 Elsevier Inc. All rights reserved. (c) SEM image of FeLDH(FeCo)/$Co(OH)_2$-2. (d) HRTEM image of Fe LDH(FeCo)/$Co(OH)_2$-2.[116] Copyright © 2019 Wiley-VCH Verlag GmbH & Co. KGaA, Weinheim. (e) TEM image of CuO_x@CoO NRs. (f) LSV curve of the catalyst in 1.0 KM KOH and (g) the corresponding Tafel slope graph.[117] Copyright © 2020 Wiley-VCH Verlag GmbH & Co. KGaA, Weinheim.

of the porous nanoarray. Unlike ZIF-67 grown *in situ*, Zhao *et al.*[116] used an ion-exchange method to gradually convert 2D-ZIF-67 grown on carbon cloth to $Co(OH)_2$, and then prepared the layered Fe LDH (FeCo)/$Co(OH)_2$ array (Fig. 10c and d). The ion exchange method can replace the subsequent high-temperature carbonization process of MOFs to a certain extent. Yu *et al.*[117] first synthesized vertically grown $Cu(OH)_2$ nanorods on copper foam. Rod-shaped $Cu(OH)_2$ is used as a template to obtain $Cu(OH)_2$@ZIF-67 precursor on CF (Fig. 10e). After heat treatment, a layered CoO polyhedron-modified CuO_x heterojunction nanorod array was obtained on CF. Benefiting from convenient electron transport between CuO_x and CoO, CuO_x@CoO NRs/CF showed considerable catalytic activity (Fig. 10f and g). Compared with the $MnCo_2O_4$@Co_3O_4 electrocatalyst prepared *ex situ* by Han and others,[118] the catalyst prepared *in situ* showed a relatively good catalytic performance.

The nanoarray architecture has a unique hierarchical structure, large surface area, a large number of active sites, convenient electron migration and mass transfer, close interface contact, and rapid bubble release, so it has excellent electrocatalytic activity and durability. Li *et al.*[88] found through simulation calculations that the vertically arranged array structure could guide the uniform distribution of ion currents, so more catalytically active sites could be used more effectively, thereby promoting OER catalysis. It shows that the OER catalytic performance of the array structure has an outstanding performance (Table 4 and Fig. 11). Since the array structure can guide the uniform distribution of the ion current, it can use more catalytically active sites more effectively, so it exhibits better performance than other structures. Moreover, it still has an excellent catalytic performance at a high current density, and thus, is expected to be a catalyst for industrial production. Although great progress has been made in designing the structure of nanoarrays, enhancing the electrocatalytic performance is still a huge challenge, especially in ZIF-67 based catalysts. For effective and stable electrocatalytic water splitting, the catalytic performance of the catalyst can be improved by changing the composition, morphology, size, and interface of the catalyst and introducing dopants or defects. In addition, there is an urgent need to accurately prepare nanoarray structures on different conductive substrates.

4 Doping

The catalytic performance can be improved by carbonization at high temperature without destroying the structure of ZIF-67. In recent years, M–N–C materials have shown excellent performances in the application of electrochemical water splitting, and the presence of certain metals (such as Co) can promote the formation of structures such as CNTs. In addition, metal intercalation, N doping, and synergistic effects (adjustable H-bond energy and conductivity) all help to improve electrocatalytic performance.[121–123]

Table 4 Comparison of different array catalysts based on ZIF-67 and its derivatives

Array	Substrate	Electrolyte	Overpotential/mV	Tafel/mV dec^{-1}	Current density/mA cm^{-2}	Ref.
Fe LDH(FeCo)/$Co(OH)_2$	CC	1 M KOH	242/279	34.4	10/100	116
Co_3O_4@Ni_2P–CoP/NF	NF	1 M KOH	250/298/320	75	10/50/100	119
Ni@CoO@CoNC	NF	1 M KOH	309/420	53	10/100	115
$MnCo_2O_4$@Co_3O_4	NF	2 M KOH	170/280	109.6	10/100	59
CuO_x@CoO NRs/CF	NF	1 M KOH	254/334	56.9	10/100	117
Co–Ni_3S_2/NF	NF	1 M KOH	120/240	38.4	10/100	120

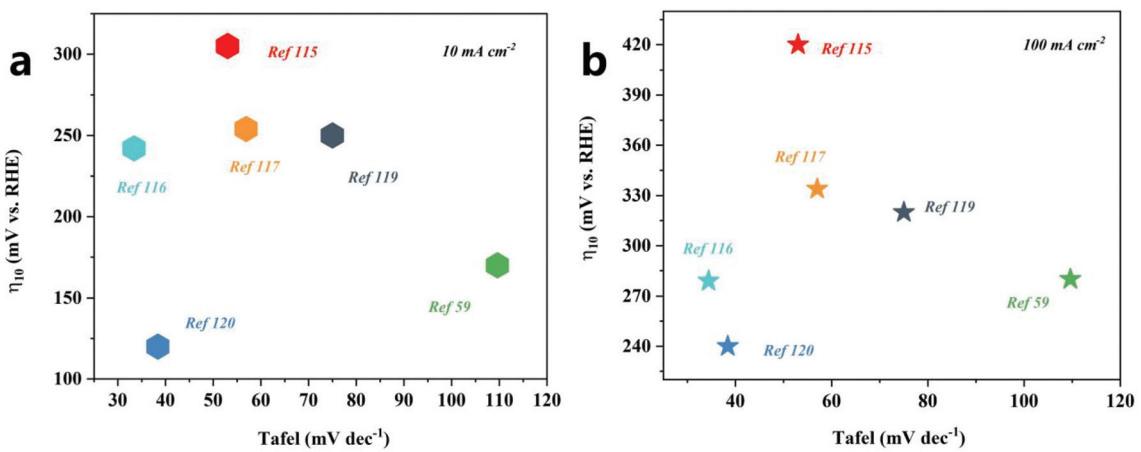

Fig. 11 OER activity comparison graph showing the Tafel slopes versus overpotential at current densities of 10 mA cm^{-2} (a) and 100 mA cm^{-2} (b) for different catalysts.

4.1 Anion doping (AD)

The introduction of anions such as P, N, S, O or F with different atomic sizes and electronegativity into the matrix material will cause lattice distortion, thereby adjusting the electronic structure and catalytic activity. In addition, the synergistic effect between metal nanoparticles and heteroatoms also helps to improve electrocatalytic performance, and heteroatoms doped into the carbon framework can also help to activate π electrons by destroying the integrity of p-conjugation, thereby improving the electrocatalytic activity.[124,125]

For example, Ni *et al.*[51] designed a self-sacrificing template strategy, using the ZIF-67 dodecahedron and hexamethylenetetramine as reactants to synthesize hollow α-$Co(OH)_2$ nano-dodecahedra. Experiments show that the prepared α-$Co(OH)_2$ (hollow nano-dodecahedron) material has an excellent OER catalytic activity. In addition, under the same conditions, Cl-doped α-$Co(OH)_2$ hollow nano-dodecahedra can also be prepared. The α-$Co(OH)_2$ hollow nano-dodecahedron doped with Cl showed better OER activity. Catalysts doped with Cl atoms are easily etched under electrochemical conditions (Fig. 12a–c). Thus, introducing vacancies and defects improves the OER catalytic performance of α-$Co(OH)_2$ hollow nano-dodecahedra. In addition, Zhang *et al.*[126] prepared a Br-doped catalyst (BrHT@CoNC) through self-sacrifice and pyrolysis. Br doping will cause charge polarization, thereby promoting electron transfer, which will benefit OER catalysis. In addition, the defects introduced by Br doping are also beneficial to the catalytic process of the OER.

Anion regulation, that is, modulating the electronic structure of the cation active site through the anion environment of the transition metal compound can effectively improve the catalytic activity of the catalyst. Precise anion regulation is expected to construct an ideal anion structure, thus presenting the best intrinsic catalytic activity. However, precise anion control is still very difficult, and new anion control strategies need to be developed.[127,128]

4.2 Cation doping (CD)

To optimize the local electronic environment and increase the catalytic activity, the introduction of anion vacancies can lead to the formation of high-energy dangling bonds and low coordination sites, thereby promoting OER catalytic reactions. In addition, CD is also a way to improve conductivity and reduce the binding energy of intermediate products, and it can be found that the d-band doping of transition metal elements can also effectively improve the catalytic performance of the OER. That is, the doping of transition metal elements improves the catalytic process of the OER by adjusting the electronic structure, adjusting the redistribution of charges, and so on. For example, Liu *et al.*[129] have reported a new type of OER catalyst: Fe-$Co_{1.11}Te_2$@NCNTF (NCNTF: nitrogen-doped carbon nanotube framework). The catalyst is synthesized by tellurizing the catalyst obtained after Fe^{3+} etching of ZIF-67 in H_2/Ar gas. The improved electrocatalyst (Fe-$Co_{1.11}Te_2$@NCNTF-2) shows excellent OER catalytic performance (107 mV@10 mA cm^{-2}) in 1M KOH. However, undoped Fe $Co_{1.11}Te_2$@NCNTF showed an overpotential of 165 mV, which indicated that Fe doping could adjust the electronic structure of the catalyst and promote the OER reaction kinetics, thereby improving the catalytic performance (Fig. 13a and b).

Mu *et al.*[130] proposed a simple and practical method based on a metal–organic framework to prepare iron-doped cobalt phosphide ($Fe_{0.27}Co_{0.73}P$). Through Fe doping, the obtained electrocatalyst ($Fe_{0.27}Co_{0.73}P$/NF) coated on Ni foam substrate has an excellent OER performance (η_{10} = 251 mV). In addition, when $Fe_{0.27}Co_{0.73}P$/NF is used as a symmetric electrode in 1.0 M KOH alkaline solution, it also has an excellent OER catalytic performance (1.68 V@10 mA cm^{-2}). In addition, a small amount of iron that failed to enter the cobalt phosphide lattice is phosphated (Fig. 13c and d). This phosphated iron facilitates the redistribution of charges, thereby promoting the OER performance of the electrocatalyst. In addition, Lou *et al.*[131] prepared a layered cross-channel hollow NP composed of ultra-thin Co_3O_4 nanosheets by an etching–coordination–recombination method. The advantage of this method is also that it permits the simultaneous introduction of a second metal. In general, metal elements can be doped into ultra-thin Co_3O_4 nanosheets in the form of isolated metal sites (Fig. 13e and f). For example, doping with Fe atoms at the octahedral site of Co_3O_4 greatly enhances the intrinsic electrical activity of the catalyst, and all doped Fe atoms should exist near the surface. Therefore, it is easy to understand that, as shown by the DFT

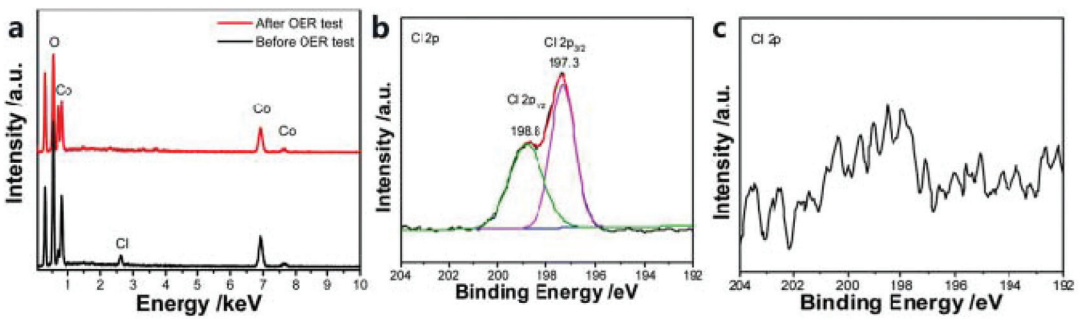

Fig. 12 (a) EDS analysis of Cl-doped α-$Co(OH)_2$ catalyst in 1 M KOH solution. Cl 2p XPS spectra of the catalyst before OER test (b) and after the OER test (c).[51] Copyright © 2019, Royal Society of Chemistry.

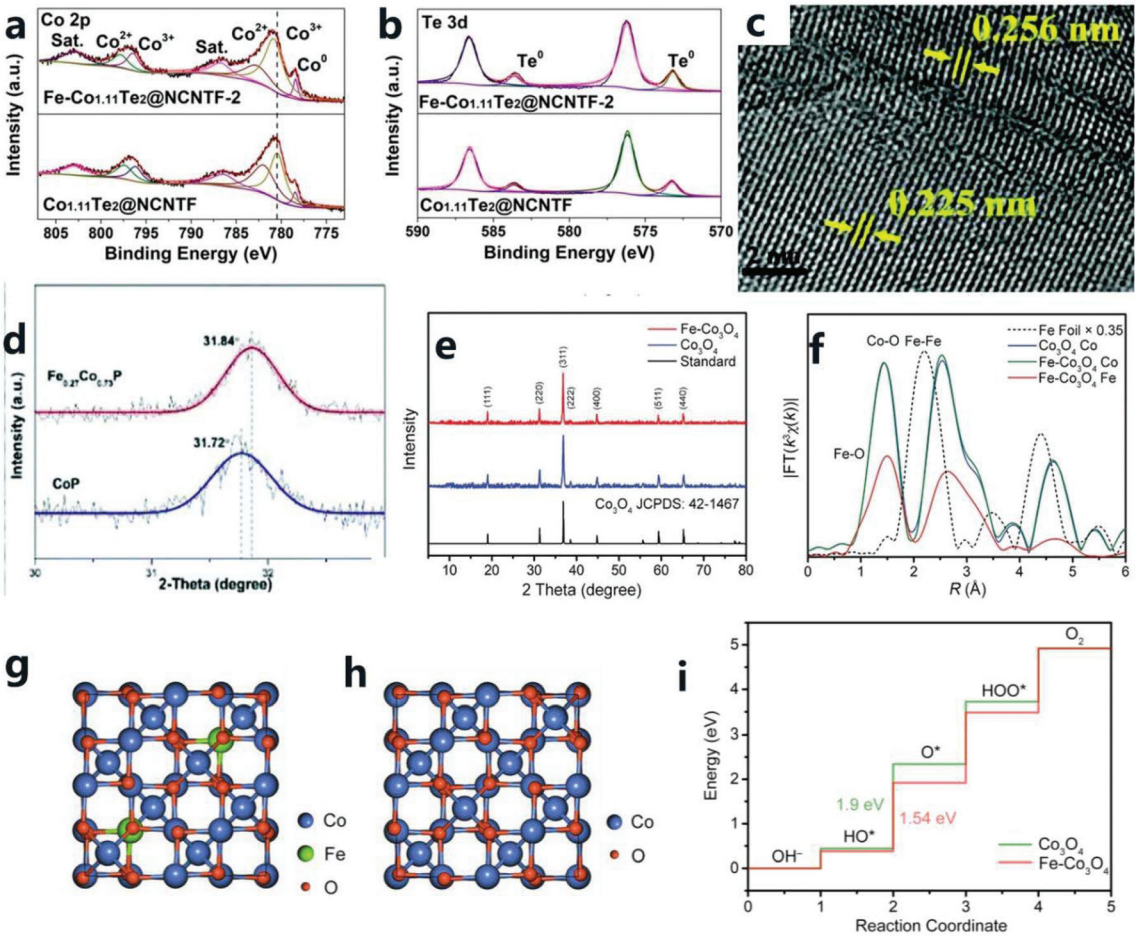

Fig. 13 Comparison of the XPS spectra of (a) Co 2p and (b) Te 3d in $Co_{1.11}Te_2$@NCNTF and Fe-$Co_{1.11}Te_2$@NCNTF-2.[129] Copyright © 2020 Wiley-VCH GmbH. (c) HRTEM image of $Fe_{0.27}Co_{0.73}P$. (d) XRD patterns for slow scanning at one degree per minute. (e) XRD patterns of Co_3O_4 HHNPs and Fe–Co_3O_4 HHNPs together with the standard pattern of Co_3O_4.[130] Copyright © 2019, Royal Society of Chemistry. (f) FT of EXAFS $k3\chi(k)$ spectra of Fe–Co_3O_4 with Fe foil and Co_3O_4 as references. (g) The optimized Fe–Co_3O_4 structure for calculation. (h) Crystal structure of Co_3O_4. (i) Free energy diagram for the OER process over Co sites.[131] Copyright © 2020 The Authors. Published by Wiley-VCH Verlag GmbH & Co. KGaA, Weinheim.

results, even a small amount of Fe atom doping will greatly enhance the electrocatalytic activity (Fig. 13g–i).

It is certain that the incorporation of iron plays an important role in improving OER catalysis. However, the enhancement of the electrocatalytic activity by single metal doping is still limited. In addition, the electronic structure and the adsorption of intermediates can be optimized due to doping with various metal ions. Therefore, the combined doping with multiple metal ions will be a promising method for water splitting.[132] Studies have shown that the simultaneous incorporation of two foreign cations can more effectively adjust the lattice structure and electronic interaction, thereby further improving the catalytic performance.[133]

4.3 Co-doping (CoD)

4.3.1 Sulfur–nitrogen CoD. Currently, sulfur/nitrogen co-doped carbon catalysts have been extensively studied. In particular, the CoD process may introduce more heteroatoms into the carbon skeleton to promote the catalytic activity. Although there is no charge transfer between S and C, they have similar electronegativity, and it can be found that S/C doping can increase the charge/spin density. For example, Huang *et al.*[134] prepared a catalyst with excellent OER catalytic activity through sulfur and sulfur co-doping. It is worth noting that the presence of sulfone and sulfite groups (high binding energy) in the graphene layer plays a very important role in enhancing the catalytic performance of the OER. In addition, this synergy between nitrogen-doped carbon and sulfur-doped cobalt oxide can effectively improve the performance of the catalyst. In addition, Cheng *et al.*[135] used a simple method to pyrolyze sulfur-doped ZIF-67, and then obtained a catalyst in which Co–CoO nanoparticles were encapsulated in a carbon shell co-doped with N and S (Fig. 14a and b). Adding thiourea *in situ* to ZIF-67 not only reduces the size of Co–CoO nanoparticles, but also adjusts the electronic structure of Co–O–C and Co–N4 to improve its OER catalytic performance. In addition, DFT calculations show that the S-doped catalyst can reduce the *OOH binding energy between the Co–N4 position and the Co–O–C

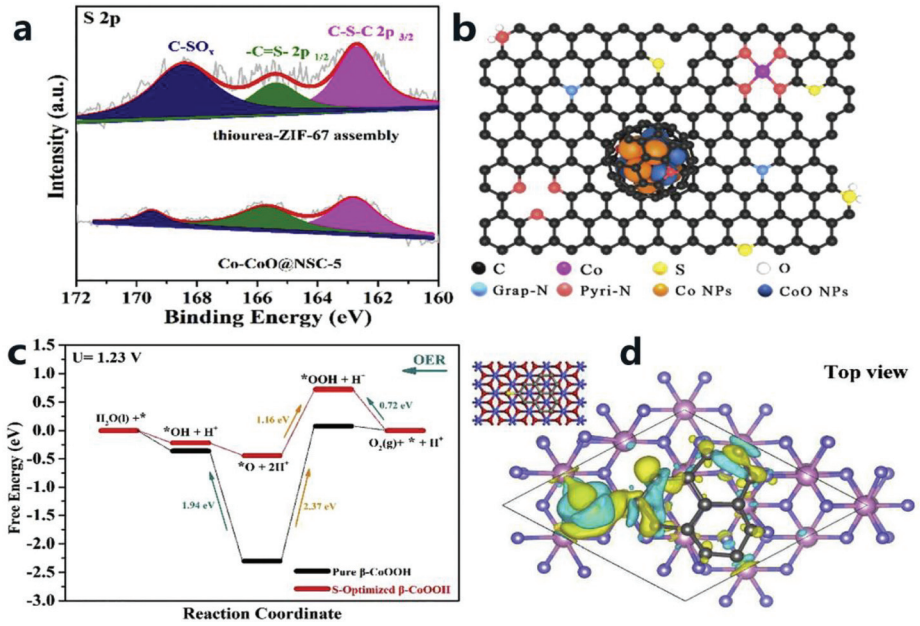

Fig. 14 (a) S 2p XPS spectrum of thiourea–ZIF-67 component and Co–CoO@NSC-5. (b) Microscopic diagram of Co–CoO@NSC-5. (c) The calculated free-energy diagram of the OER on S-optimized β-CoOOH (001) (U = 1.23 V). (d) The spin charge density distribution of β-CoOOH (001) (top view). Yellow indicates spin up and cyan indicates spin down.[135]

bond during the OER reaction, thereby improving the performance of the catalyst (Fig. 14c and d).

4.3.2 Phosphorus–nitrogen CoD. P-Substituted graphene and *N*-substitution are more important than the corresponding materials in the anti-substitution sequence for determining better crystallinity and conductivity and good element mixing. This may be another strategy for researchers to design metal-free catalysts.

Jin *et al.*[136] used H_3PO_4 to selectively etch ZIF-67 to synthesize a P/N co-doped carbon catalyst material (Co/P/N–CNP) with micro/mesomicropores. H_3PO_4 not only effectively controls the porosity of ZIF through etching, but also is an ideal phosphorus source for P doping, which effectively improves the performance of the catalyst. The Co/P/N–CNP catalyst obtained after pyrolysis is modified with multi-walled carbon nanotubes and has both micropores and mesopores, which are beneficial for exposing more reactive sites during OER electrocatalysis.

In the anion adjustment process, some of the original anions are replaced with foreign anions to obtain polyanionic compounds. The obtained polyanionic compound has a heteroatom structure, polarized and non-polarized anions with atom distribution. The dispersed electrons of the polarized anion are shared with adjacent cations, thereby adjusting the covalent and ionicity of the interaction between the cation and anion. Non-polarized anions are mainly ionic, with weak electronic interaction. The polarized sulfur anion and the non-polarized oxyanion coordinately adjust the electronic structure of the active site through the electronic interaction with the cation. Through anion adjustment, the degree of polarization of the cation active site can be fully adjusted through the

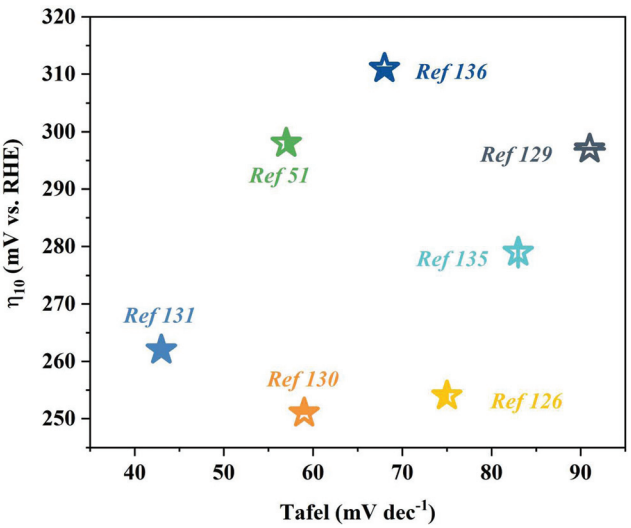

Fig. 15 OER activity comparison graph showing the Tafel slope versus overpotential at a current density of 10 mA cm^{-2} for different catalysts.

heteroatom structure, thereby generating a favorable electronic structure for effective electrocatalysis. In addition, the CoD strategy for cations and anions is very attractive because it may cause a double synergistic effect in adjusting the electronic structure and changing the adsorption energy during the reaction to promote the catalytic performance. In addition, we compared the catalytic performance of different ion-doped catalysts (Fig. 15). Many nanostructures benefit from the structural tunability and synergistic effects of dopants. Therefore, in addition to studying structure regulation and doping separ-

ately, we should also explore the synergistic effects between them to combine their respective advantages for improved catalyst performance.

5 ZIF-67 derived single atom catalyst

The special structure of a MOF can be transformed into a single-atom electrocatalyst with high activity and the M–N_x–C structure by improving the physical design of a MOF to increase the catalytic efficiency of water oxidation. Inspired by the ultra-high utilization of single atom catalysts (SAC), MNC catalysts with atomic dispersion (especially from MOFs) are currently the focus of attention from researchers. Therefore, the design of the original MOF single-atom electrocatalyst is essential. For example, Wang *et al.*[137] stabilized metal ions (Pt^{2+}/Ir^{2+}/Pd^{2+}/Ru^{2+}/Ni^{2+}/Fe^{2+}) by coordinating them with the π electron of the imidazole group of ZIF-67, thereby anchoring an isolated single-atom on the imidazole group of ZIF-67, to obtain a catalyst composed of N-doped carbon matrix and metal nanoparticles through a simple pyrolysis process. Then, through experiments and DFT calculations, it can be found that the high accessibility of the numerous tunnels in the ZIF-67 framework disperses individual atoms, thereby greatly increasing the density of active sites.

In addition, Wang *et al.*[138] used plasma etching (DBDPT) to remove the partial distribution of ZIF-67 and generate coordinatively unsaturated metal sites (CUMS) for electrochemical catalysis. By adjusting the geometric ligands to produce CUMS, Co ions are converted into active catalytic centers (Fig. 16a). In addition, CUMS formed by plasma etching can be used to remove organic ligands for OER catalysis. The specific structure of the catalyst and monodisperse CUMS after etching lead to an excellent OER catalytic performance (Fig. 16b). DFT calculations confirmed that the unsaturation of the catalyst after etching could effectively improve the activity of the catalyst (Fig. 16c). In addition to the method of etching the ligand, Dilpazir *et al.*[139] used dicyandiamide modification to prepare CoSAs@NCNT single-atom catalysts (Fig. 16d–g). This catalyst with Co atom-immobilized CNTs exhibits excellent OER performance. Combining melamine with a carbon matrix promotes the formation of carbon nanotubes, and the formation rate of carbon nanotubes is controlled by the autocatalysis of cobalt nanoparticles (Fig. 16h). In addition, it can also be found that the nitrogen-rich DCD is responsible for the generation of stable Co single-atom sites. Nitrogen in the DCD surrounds the Co site, thus limiting the formation of aggregated nanoparticles. Recently, Sun and others[140] prepared a single Co atom catalyst (UNT Co SAs/NC) (Fig. 16i and j) with a urchin-like hierarchical structures and a precise arrangement through a simple MOF template method. The prepared catalyst has an excellent catalytic performance due to its unique single-atom characteristics (Fig. 16k). In addition, the consistency between DFT calculations and experiments shows that

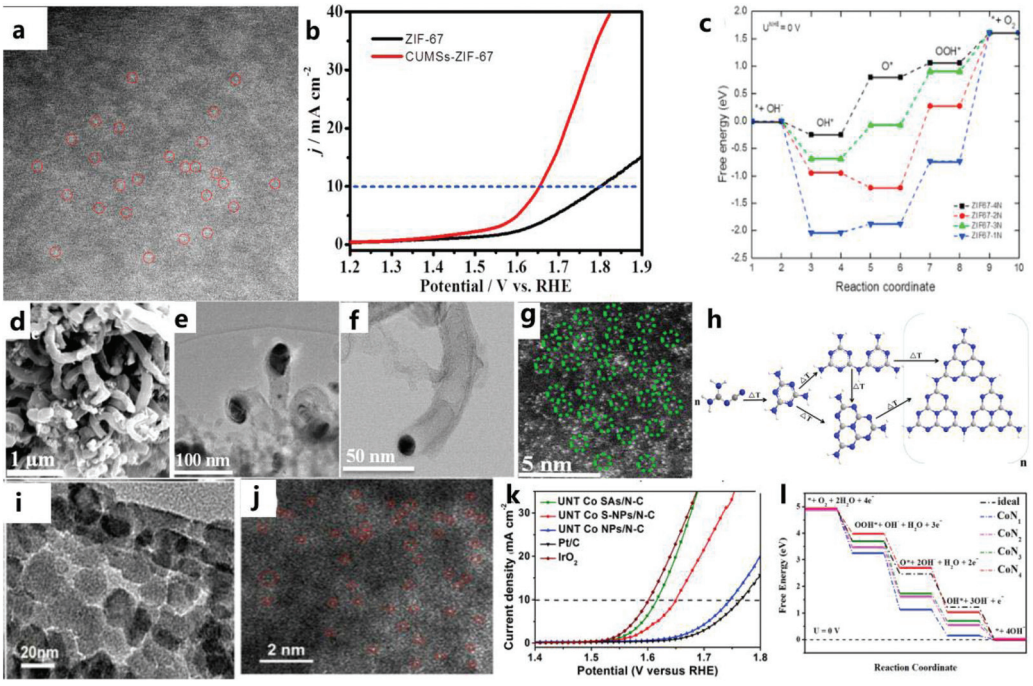

Fig. 16 (a) Corresponding SAED pattern of CUMS-ZIF-67. (b) LSV polarization curves of ZIF-67 and CUMS-ZIF-67 electrocatalysts. (c) Free energy diagrams of ZIF-67-*x*N (*x* = 1–4).[138] Copyright © 2017 Elsevier Ltd. All rights reserved. (d) SEM image of CoSAs@CNTs. (e) TEM image of CoSAs@CNTs. (f) HAADF image of CoSAs@CNTs. (g) HAADF image showing the atomic distribution of cobalt atoms. (h) Schematic illustration of the growth mechanism of CNTs.[139] Copyright @ 2018, American Chemical Society. (i) TEM image of hierarchical UNT Co SAs/N–C catalyst. (j) HAADF-STEM image of hierarchical UNT Co SAs/N–C catalyst. (k) OER polarization curve of the catalyst. (l) Free-energy diagrams for OER pathways in an alkaline medium on CoN*x* (*x* = 1–4) active sites.[140] Copyright © 2019 Elsevier Ltd. All rights reserved.

UNT Co SA/NC with CoN_4 can effectively improve the performance of OER catalysts (Fig. 16l).

In short, ZIF-67 has unique π electrons in the imidazole pentagon, which can be used as an aggregation inhibitor, and the unique coordination environment facilitates the preparation of single-atom catalysts.

6 Compound catalyst of ZIF-67 derivatives

Compared with the original ZIF-67 material, the ZIF-67 derived composite catalyst maintains the advantages of ZIF-67's high specific surface area and large porosity, which can provide more active sites for the catalytic process, and after carbonization and various subsequent treatments, the electron transport efficiency of the catalyst is improved, thereby improving its catalytic performance. Besides pristine ZIF-67 and their derived porous carbons, ZIF-67 can also be converted into metal oxides, metal phosphides, chalcogenides, *etc*. under certain conditions. The special combination of the metal center and organic complex in ZIF and its heat treatment, as well as the feasible introduction of the second precursor, will introduce more active sites to improve the performance of the catalyst. In addition, due to some shortcomings of ZIF-67 and its derivatives, the OER catalytic performance is limited. We can make up for these shortcomings by doping and compounding to improve the catalytic performance. This synergistic effect improves the catalytic performance through a similar synergistic chemical coupling effect.[141]

6.1 ZIF-67 derived transition metal oxide catalyst (ZDMOC)

As a low-cost alternative, a composite of transition metal oxide and carbon materials shows catalytic activity for the OER.[142] Generally, a transition metal oxide is considered to be the main catalyst for the OER.[143] The MOF is a type of porous material assembled from metal ions and organic linkers and has become the main focus of nanoscience.[144,145] In particular, MOFs can be used as a self-sacrificing template to prepare porous transition metal oxide or metal/N-doped carbon materials. Due to the unique structure of the MOF, the derived material has a large surface area and a layered porous structure, which are necessary for the high-performance OER process.[146,147]

For example, Luo *et al.*[148] prepared catalysts with different structures (Co_3O_4/NPC) by controlling the pyrolysis of different ZIF-67 precursors (Fig. 17a–c). Catalysts with different structures exhibit different catalytic performances. In addition, due to the large number of defects in the amorphous catalyst, this can provide a larger number of OER active sites compared with the crystalline catalyst. For example, Pang *et al.*[149] prepared catalysts with different crystalline morphologies by heat-treating ZIF-67 hollow spheres by controlling the temperature (Fig. 17d). Through electrochemical testing, it can be found that the catalytic activity of the amorphous Co_3O_4 catalyst is better than that of the crystalline catalyst (Fig. 17e).

In addition, designing multiple composites of M–Co compounds further improves the catalytic performance.[102,150] Recently, studies have shown that Mo can effectively cooperate with Co, and has led to great progress in this field.[151] For example, Chen *et al.*[45] prepared a catalyst with a special structure of nanorods and nanoparticles (Fig. 17f–h). The cooperative interaction between CMO nanorods and CoO_x nanoparticles can achieve efficient charge transfer and promote electrocatalytic OER processes (Fig. 17i).

6.2 ZIF-67-derived transition metal phosphide catalyst (ZDMPC)

In recent years, due to the attractive performance of nanostructured metal phosphides in electrocatalytic applications, extensive research has been conducted on them. Metal phosphides are a type of electrocatalyst used in the OER.[152–154] Although some progress has been made, the OER performance of metal phosphides still needs to be improved. For example, Li *et al.*[155] successfully prepared the CoNiP/NC catalyst (Fig. 18a and b) as an effective electrocatalyst for the OER using the common method of phosphating (*i.e.*, annealing NaH_2PO_2 and catalytic materials under an inert atmosphere). Among the electrocatalysts obtained by controlling the carbonization and phosphating temperature, the CoNiP/NC700 catalyst (where 700 represents the calcination temperature (°C)) exhibits excellent electrocatalytic activity for the OER. In addition, the CoNiP/NC electrocatalyst obtained at 700 °C has a superior OER catalytic performance to those of Co/NC and CoNi/NC (Fig. 18c). Among them, the better electrocatalytic activity of hybrid materials can be attributed to the strong electronic coupling effect of Co, Ni, P, and C. In addition to the above-mentioned commonly used method of phosphating, Jin *et al.*[136] also selectively corroded the ZIF-67 precursor with H_3PO_4, and then pyrolyzed it to obtain the Co/P/N–CNP catalyst (Fig. 18d and e). This method not only effectively controls the porosity of ZIF, but can also effectively dope P into the carbon matrix. P greatly enriches the electrocatalytically active sites of the obtained carbon catalyst.

6.3 ZIF-67-derived transition metal sulfide catalyst (ZDMSC)

Transition metal sulfides are widely studied as promising electrocatalysts due to their high abundance, low cost, and excellent electrocatalytic activity.[156–158] In recent years, due to abundant raw materials, environmental protection characteristics, and excellent performance of MOF derivatives, they have received extensive attention from researchers.[159,160] Studies have shown that the effect of S on metal active sites for the OER is similar to that of P.[161] Therefore, in recent years, people have used the ZDMSC catalyst for OER electrocatalysis. In addition, there is a synergy between the nanoscale interfaces of different transition metal catalysts, which will further enrich structural defects and stimulate some inert sites, thereby increasing the activity of the two transition metal catalysts. For example, Yang and others[162] first introduced the preparation of Co–Ni–S co-doped N-enriched ($CoNi_xS_y$/NCP) through an absorption–pyrolysis–sulfurization method

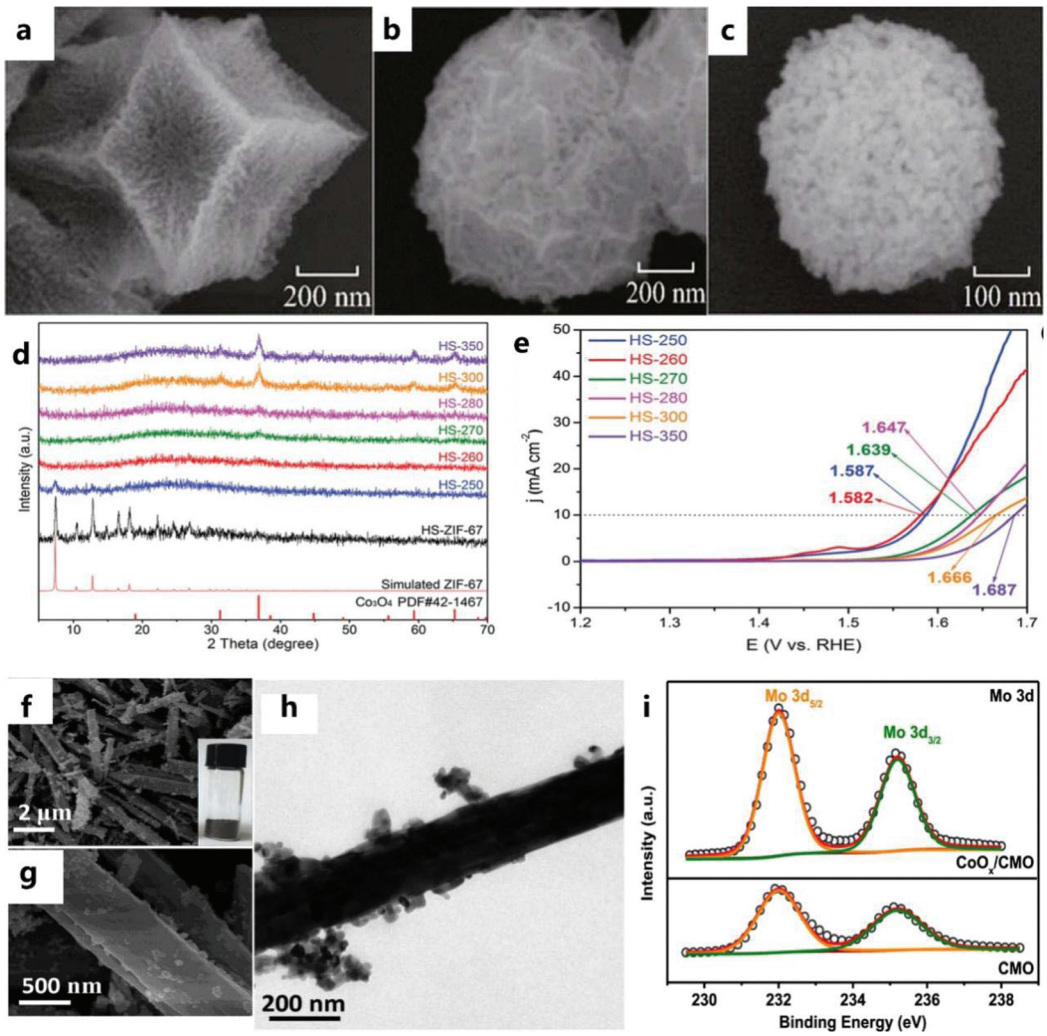

Fig. 17 (a) SEM images of T-Co_3O_4/NPC, (b) M-Co_3O_4/NPC, (c) and H-Co_3O_4/NPC.[148] Copyright @ 2017,The Author(s). (d) XRD patterns of all samples. (e) LSV curves of HS-250, HS-260, HS-270, HS-280, HS-300, and HS-350.[149] Copyright © 2019 Wiley-VCH Verlag GmbH & Co. KGaA, Weinheim. (f and g) TEM images of CoO_x/CMO. Inset is a picture of the as-prepared sample. (h) TEM image of CoO_x/CMO. (i) High-resolution Mo 3d XPS spectra of CoO_x/CMO-p and CoO_x/CMO.[45] Copyright © 2019 Elsevier B.V. All rights reserved.

(Fig. 19a and b), and it can be seen that the performance of the catalyst after vulcanization has been significantly increased (Fig. 19c). Compared with pyrolysis vulcanization, Zhang *et al.*[163] used a more convenient and energy-saving ion exchange method to prepare amorphous CoS_x@C, that is, amorphous CoS_x@C was calcined under Ar at 400 °C to obtain $Co_{1-x}S$@C. The $Co_{1-x}S$@C catalyst (Fig. 19d) showed an effective OER activity (Fig. 19e). The excellent electrical conductivity of $Co_{1-x}S$@C (Fig. 19f), the porous structure that promotes mass transfer, and the uniform dispersion of $Co_{1-x}S$@C particles throughout the carbon skeleton lead to an excellent catalytic performance.

6.4 ZIF-67-derived transition metal selenide catalysts (ZDMSeC)

Both selenium and transition metals have d orbitals, and the 3d–2p repulsion between them results in faster delivery of dioxygen intermediates, thereby increasing the OER activity.[161] For example, Tian *et al.*[49] used a convenient hydrothermal method to construct high-performance nanovesicle $CoSe_2$ electrode materials. Then, by adjusting the stoichiometric ratio of Co and Se, they studied the nanovesicle $CoSe_2$ in detail. It can be found that the best $CoSe_2$-30 catalyst (Fig. 20a) has an excellent OER performance. Fig. 20b illustrates the presence of Co_2^+ and Co^{3+}, and Fig. 20c demonstrates the formation of cobalt selenide on the surface of the electrocatalyst. It can be seen that selenium and cobalt do interact. Wei *et al.*[164] prepared Ni–Co–Se dodecahedral nanocage catalysts by selenization (Fig. 20d), and the synergistic combination of $Co_{0.85}Se$ and $Ni_{0.85}Se$ in the nanocage may help to improve the catalytic activity. Similarly, Fig. 20e and f demonstrate the formation of cobalt selenide on the surface of the electrocatalyst. The abovementioned results all indicate that the yolk–shell Ni–Co–Se nanocage/CFP electrode has an excellent electrocatalytic performance under alkaline conditions.

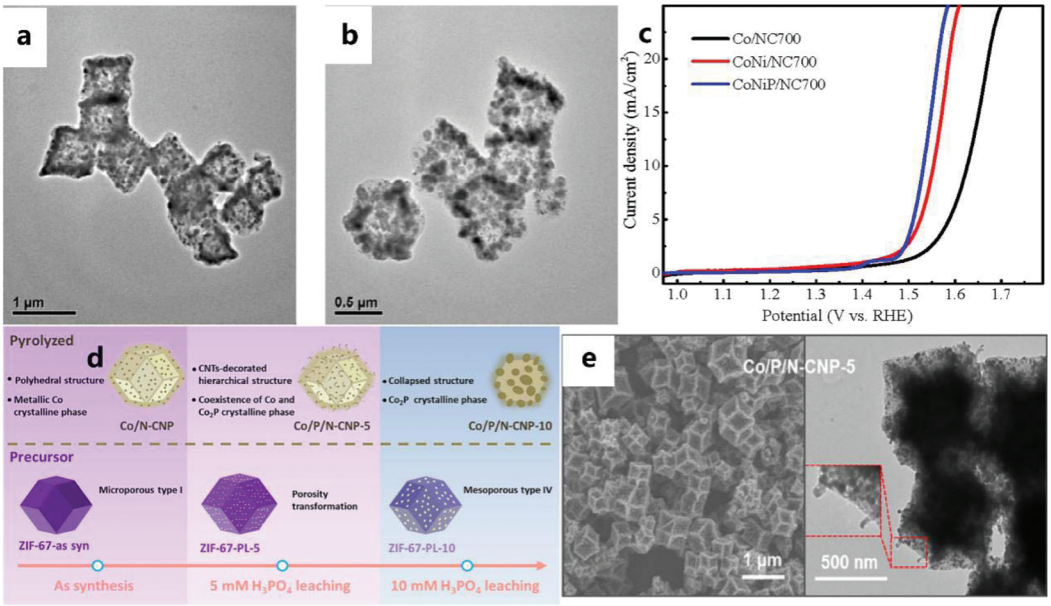

Fig. 18 (a) TEM images of CoNi/NC700 and (b) CoNiP/NC700. (c) Polarization curves in KOH solution.[155] Copyright © 2018 Dalian Institute of Chemical Physics, the Chinese Academy of Sciences. Published by Elsevier B.V. All rights reserved. (d) Schematic illustration of a pre-leaching strategy for the preparation of Co/P/N–CNP catalysts. (e) SEM and TEM images of Co/P/N-CNP-5.[136] Copyright © 2020 Elsevier Ltd. All rights reserved.

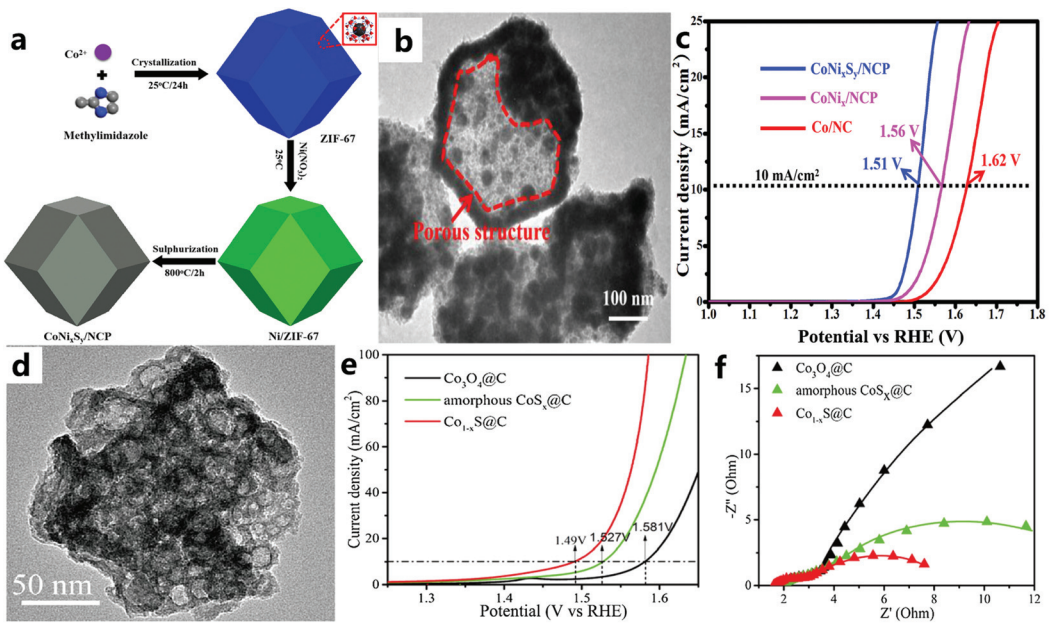

Fig. 19 (a) Schematic diagram for the fabrication of $CoNi_xS_y$/NCP. (b) TEM image of $CoNi_xS_y$/NCP. (c) Polarization curves of Co/NC, $CoNi_x$/NCP, and $CoNi_xS_y$/NCP in 1 M KOH solution (scan rate: 10 mV s^{-1}).[162] Copyright © 2019 Hydrogen Energy Publications LLC. Published by Elsevier Ltd. All rights reserved. (d) TEM image of $Co_{1-x}S$@C. (e) LSV polarization curves of Co_3O_4@C, $Co_{1-x}S$@C, and amorphous CoS_x@C. (f) EIS Nyquist plots of Co_3O_4@C, $Co_{1-x}S$@C, and amorphous CoS_x@C.[163] Copyright © 2018 Published by E.V. on behalf of Chinese Chemical Society and Institute of Materia Medica, Chinese Academy of Medical Sciences.

6.5 ZIF-67-derived transition metal telluride catalyst (ZDMTC)

Because tellurium is very similar to sulfur and selenium, it is extremely valuable to study the role of tellurium in catalysis. For example, Wang *et al.*[165] encapsulated $CoTe_2$ in a nitrogen-doped carbon nanotube framework (called $CoTe_2$@NCNTFs) through a tellurization process under a hydrogen atmosphere (Fig. 21a and b). ZIF-67 converts its organic ligands into a nitrogen-doped carbon nanotube framework (NCNTF) through

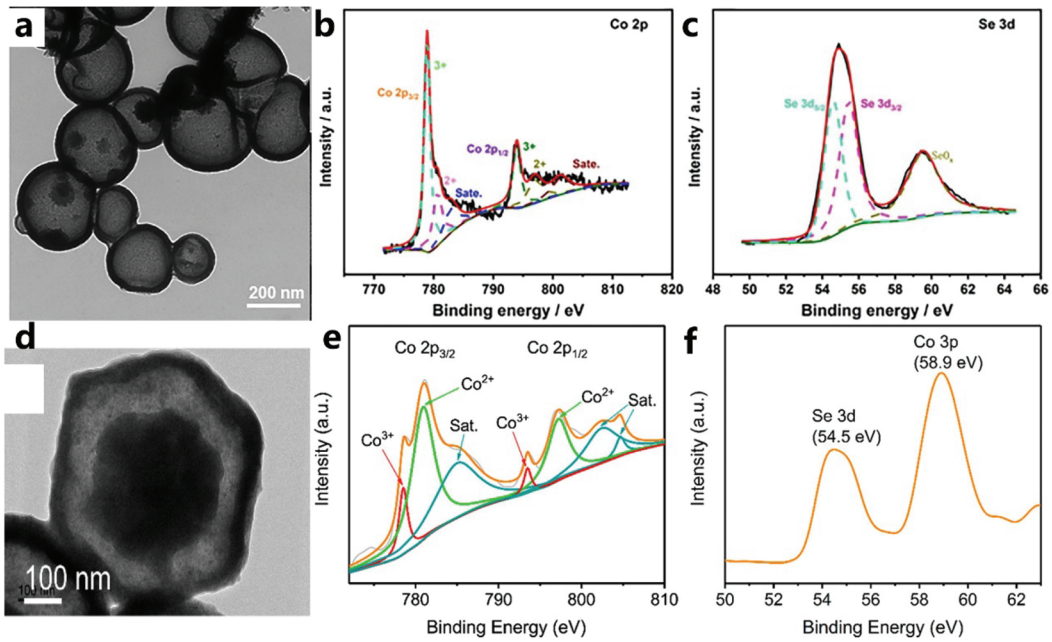

Fig. 20 (a) TEM image of $CoSe_2$-30. (b) Co 2p and (c) Se 3d XPS spectra of $CoSe_2$-30.[49] Copyright © 2019 Elsevier B.V. All rights reserved. (d) HR-TEM image of Y–S Ni–Co–Se. XPS spectra of the (e) Co 2p and (f) Se 3d regions.[164] Copyright @ 2018, American Chemical Society.

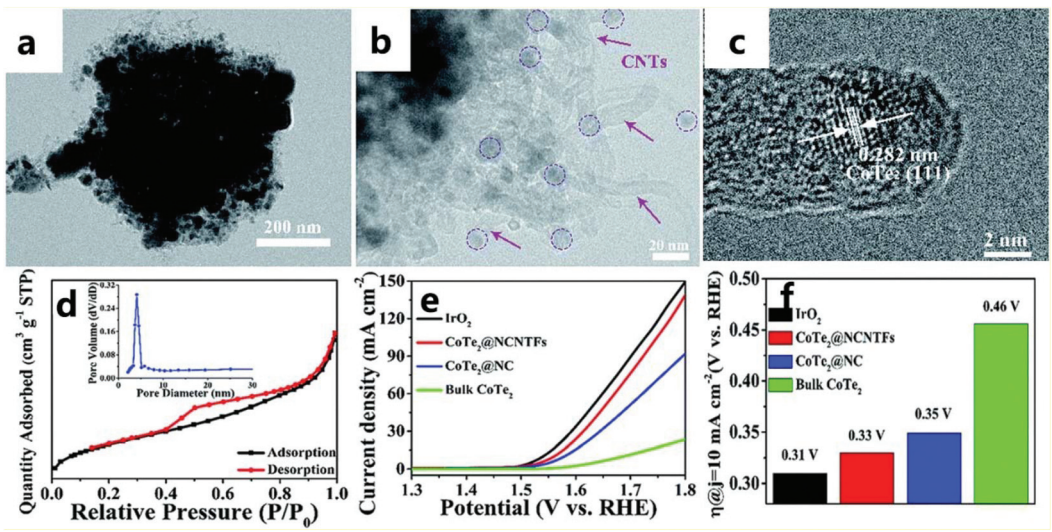

Fig. 21 (a and b) TEM images of $CoTe_2$@NCNTFs. (c) HRTEM image of $CoTe_2$@NCNTFs. (d) N_2 adsorption–desorption isotherms and the corresponding pore size distribution (inset) of $CoTe_2$@NCNTFs. (e) $CoTe_2$ polarization curves of different catalysts. (f) Histogram of the overpotential of different catalysts at 10 mA cm^{-2}.[165] Copyright © 2018, Royal Society of Chemistry.

pyrolysis, and the central metal cobalt atom forms ultrafine $CoTe_2$ nanoparticles *in situ* (Fig. 21c), so the combination of $CoTe_2$ and NCNTF leads to high stability and strong interactions. This nitrogen-doped carbon nanotube framework of ZIF-derived material can effectively increase the active sites and specific surface area of the catalyst (Fig. 21d), thereby improving the catalytic performance of the OER. When the prepared $CoTe_2$@NCNTF catalyst has a current density of 10 mA cm^{-2} in an alkaline solution (1.0 M KOH), it exhibits a high electrocatalytic performance with a high potential of 330 mV for the OER (Fig. 21e and f).

6.6 Summary

ZIF-67 can be converted into metal oxides, metal phosphides, and chalcogenides (sulfides and selenides), which show excellent OER performance (Fig. 22 and Table 5). It can be found that the overall overpotential of the vulcanized catalyst is better than that of other catalysts, and the overpotential distri-

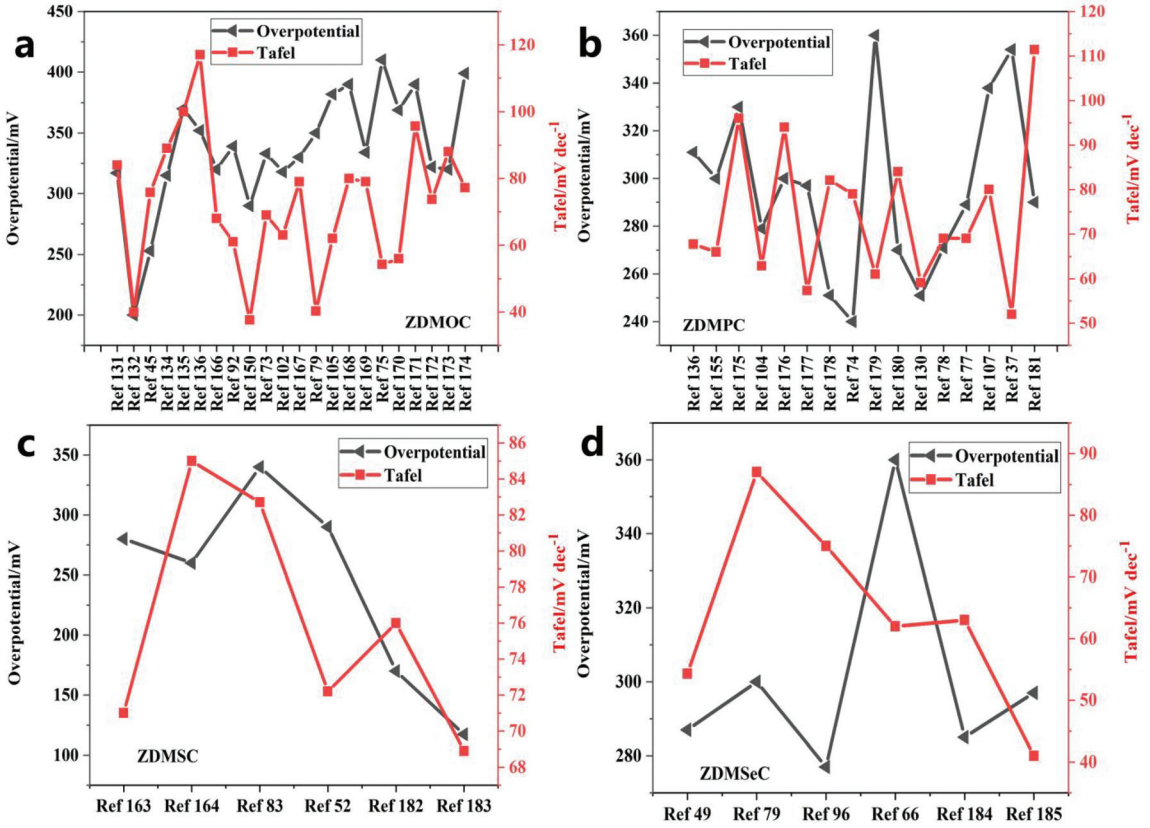

Fig. 22 Comparison of the Tafel slopes and the overpotentials of different catalysts of (a) ZDMOC, (b) ZDMPC, (c) ZDMSC and (d) ZDMSeC at a current density of 10 mA cm^{-2}.

bution has a tendency of vulcanization > phosphating > selenization > oxidation. However, the Tafel slope after vulcanization is larger, which indicates that the rate-determining step is not at the end of the multi-electron transfer reaction. The reasonably designed ZIF-67 can also be evolved into an electrocatalyst containing highly active M–N$_x$–C, which is used to improve the catalytic efficiency of water oxidation. The special combination of the metal center and the organic complex and its heat treatment, as well as the feasible introduction of a second precursor, are used to improve the efficiency of the electrocatalyst. Finally, a more in-depth understanding should be obtained and theoretical research should be conducted on the synergistic effect between the metal of the metal derivative and the carbon support, the doping effect of foreign atoms, and the phase transition in the electrochemical evolution of the ZIF-derived metal electrocatalyst. This is an indication that ZIF-67 and its derivatives are promising for the development of OER catalysts.

7 Mechanistic analysis

7.1 The catalytic activity of ZIF-67 and its favorable adsorption sites

When seeking a high-efficiency oxygen evolution electrocatalyst based on ZIF-67 materials and their derivatives, basic theoretical calculations have always played an important role in rationally designing and analyzing the performance of electrocatalysts for OER reactions. To understand the OER reaction mechanism, basic theoretical calculations based on first-principles density functional theory (DFT) have become "standard tools" for analyzing basic reaction steps.[186] For example, for the catalysis of ZIF-67, Wang *et al.*[138] used DFT methods to perform first-principles calculations to determine the electronic structure and catalytic activity of saturated and unsaturated ZIF-67. For saturated ZIF-67, the rate-limiting step in the basic reaction is the second electron transfer, and for the unsaturated reaction (x = 2–3), this is the third step of electron transfer. As shown in Fig. 23a, the top of the volcano diagram is the overpotential of the best catalyst, which is consistent with the experimental results. In addition, the Sabatier principle states that the interaction between the catalyst and the adsorbent should be moderate (not too strong or too weak). However, the amount of ligand will strongly affect the adsorption energy of the catalyst, so the amount of ligand will have a greater impact on the electrocatalytic performance of the OER. In addition, they found that the change in the charge on the metal site changes with the change in the number of ligands. The role of the ligand is closely related to the redistribution of the charge on the active site. For a metal, because it has a positive charge, it will have a strong interaction with oxygen, which

Table 5 OER catalytic performance of ZIF-67 derivative composite catalysts

ZDMOC	Substrate	Electrolyte	Overpotential/mV	Tafel/mV dec^{-1}	Current density/mA cm^{-2}	Ref.
M-Co_3O_4/NPC	GCE	1 M KOH	317	84	10	131
Co_3O_4/N-CNTs	GCE	1 M KOH	200	40	10	132
CoO_x/CMO	RDE	1 M KOH	253	75.8	10	45
$CoMoO_4$	GCE	1 M KOH	315	89	10	134
Co_3O_4-CNTs	GCE	0.1 M KOH	370	100	10	135
HS-260	GCE	1 M KOH	352	117	10	136
CO/NCO/NF	NF	0.1 M KOH	320	68	10	166
$NiCo_2O_4$/Co,N-CNTs NCs	GC-RDE	0.1 M KOH	339	61	10	92
Co_3O_{4-x}-carbon@$Fe_{2-y}Co_yO_3$	GCE	1 M KOH	290	37.6	10	150
Co_3O_4/HNCP-40	GCE	1 M KOH	333	69	10	73
Co_3O_4/$CoMoO_4$-50	GC-RDE	1 M KOH	318	63	10	102
Co_3O_4/NPC-2	GCE	1 M KOH	330	79	10	167
Co-BO@Co_3O_4	GCE	1 M KOH	350	40.3	10	79
Co_3O_4-C/rGO-W	GCD	0.1 M KOH	382	62	10	105
Co/CoO_x@NC-CNTs	RRDE	0.1 M KOH	390	80	10	168
CuO_x@CoO NRs/CF	CF	1 M KOH	334	79	100	169
Co@Co_3O_4/NC-2	GCE	0.1 M KOH	410	54.3	10	75
Ce(3)–Co_3O_4	GCE	1 M KOH	369	56	10	170
ZIF-67-CNT	GCE	1 M KOH	390	95.7	10	171
Co@NC-G-700	GCE	1 M KOH	322	73.7	10	172
MoO_2–$Co_2Mo_3O_8$@C	GCE	1 M KOH	320	88	10	173
$Ni_xCo_yO_4$/Co-NG	RDE	0.1 M KOH	399	77.2	10	174

ZDMPC	Substrate	Electrolyte	OER/mV	Tafel/mV dec^{-1}	Current density/mA cm^{-2}	Ref.
Co/P/N-CNP-5	NF	1 M KOH	311	67.7	10	136
CoNiP/NC700	GCE	1 M KOH	300	66	10	155
NiCoP/C	GCE	1 M KOH	330	96	10	175
P–CoNiFe	GCE	1 M KOH	279	62.9	10	104
NiCoPO/NC	GCE	1 M KOH	300	94	10	176
CNTs@NiCoP/C	GCE	1 M KOH	297	57.35	10	177
CNT-NC-CoP	GCE	1 M KOH	251	82.1	10	178
Co-NC@CoP-NC	GCE	0.1 M KOH	240	79	10	74
Co–P/NC/CC	CC	1 M KOH	360	61	10	179
CoP-InNC@CNT	GCE	1 M KOH	270	84	10	180
$Fe_{0.27}Co_{0.73}P$/NF	NF	1 M KOH	251	59.1	10	130
NiCoP/C@FeOOH	GCE	1 M KOH	271	69	10	78
CoP/CN@MoS_2	GC-RDE	1 M KOH	289	69	10	77
CuCoP-NC-700	GCE	1 M KOH	338	80	10	107
Co–P/NC	RDE	1 M KOH	354	52	10	37
CoP/NC-800	GCE	1 M KOH	290	111.4	10	181

ZDMSC	Substrate	Electrolyte	OER/mV	Tafel/mV dec^{-1}	Current density/mA cm^{-2}	Ref.
$CoNi_xS_y$	GCE	1 M KOH	280	71	10	163
$Co_{1-x}S$@C	platinum wire	1 M KOH	260	85	10	164
Co_9S_8@Co_9S_8@MoS_2-0.5	GCE	1 M KOH	340	82.7	10	83
CoS_2NBs-12	GCE	1 M KOH	290	72.2	10	52
NCO@CoS	NCO@CoS	1 M KOH	170	76	10	182
Mo,Co-NiS/NF-400	NF	1 M KOH	117.2/200	68.9	10/100	183

ZDMSeC	Substrate	Electrolyte	OER/mV	Tafel/mV dec^{-1}	Current density/mA cm^{-2}	Ref.
$CoSe_2$-30	GCE	1 M KOH	287	54.3	10	49
Y–S Ni–Co–Se	CFP	1 M KOH	300	87	10	79
(Co,Ni)Se_2@NiFe	GC-RDE	1 M KOH	277	75	10	96
ZIF-$Co_{0.85}Se$	GC-RDE	1 M KOH	360	62	10	66
CC/CNTs@$CoS_{0.74}Se_{0.52}$	CC	1 M KOH	285	63	10	184
$CoSe_2$/CF	CF	1 M KOH	297	41	10	185

is conducive to the adsorption of O_2, O, OH, OOH, and will become the active center for the OER.

In addition, Wang *et al.*[137] used DFT calculations to show the sites (N, Co, and C) on ZIF-67 that were conducive to metal adsorption. Metal adsorption demonstrated includes that of Pt, Pd, Ir, Ru, Fe, and Ni (Fig. 23b). It should be noted that, since the electronegativity of N is higher than that of C, more polarized electrons will be attracted to N atoms, but the deformed charge density also shows that the existence of C–C bonds and C–N bonds can redistribute the charges of all atoms in this structure. Li *et al.*[187] performed DFT calculations on Co-LDH@ZIF-67 to reveal the origin of the interface effect in the OER (Fig. 23c and d). To study the internal mechanism of electron transfer and Co–O bond strength in the catalyst (Co-LDH@ZIF-67) in depth, they calculated the projection crystal Hamiltonian (pCOHP) to illustrate the interaction of

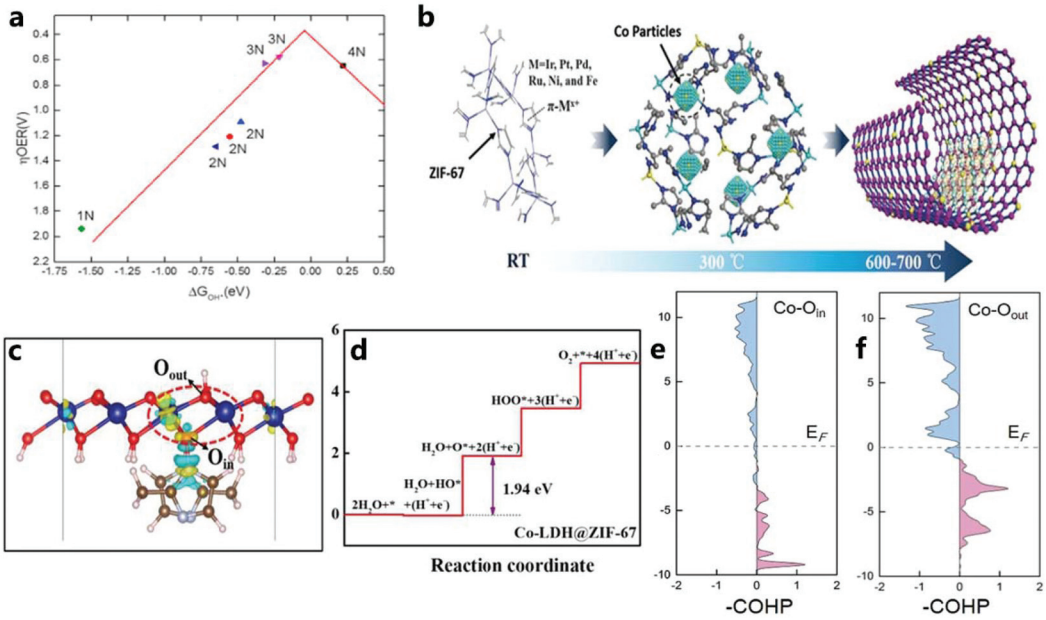

Fig. 23 (a) ZIF-67-*x*N (*x* = 1–4) volcano diagram related to the OER catalytic activity and OH adsorption energy on the Co site.[138] Copyright © 2017 Elsevier Ltd. All rights reserved. (b) Illustration of locations of metal cations and π electrons. (At room temperature, metal cations are initially related to π electrons. At 300 °C, the metal atoms embedded in cobalt form single atoms. At 600–700 °C, cobalt forms on the base carbon atom.)[137] Copyright © 2019 Wiley-VCH Verlag GmbH & Co. KGaA, Weinheim. (c) The charge density difference of the underlying layer for Co-LDH@ZIF-67, and (d) the Gibbs free energy step diagram of the OER on Co-LDH@ZIF-67. pCOHP for (e) Co–O_{in} and (f) Co–O_{out} in Co-LDH@ZIF-67.[187] Copyright © 2020 The Authors. Published by Wiley-VCH GmbH.

Co–O_{in} and Co–O_{out} (Fig. 23e and f). In addition, the decrease in free energy during the OER is due to the interaction between ZIF-67 and Co-LDH, and the decrease in antibonding orbital filling of the Co–O bond is due to the strong electron attraction of the ligand.

7.2 Catalysis of ZIF-67 derivatives

To further analyze the influence of the adsorption capacity of the intermediate on inherent catalytic activity of the catalyst, Wu *et al.*[188] performed DFT calculations on the free energy of intermediate adsorption and the charge density redistribution of C, Co@C, and Co@N_1C_{31}. First, the Co@C model is doped with nitrogen to generate an n-type doped C layer. After doping, the charge density of the Co@C–OOH system will be rebalanced, thereby further enhancing the bonding strength of C–OOH (Fig. 24a). It can be found that N-doped Co–C conjugated species can effectively change the catalytic activity of the OER. Wang *et al.*[167] calculated the geometric and electronic effects of Co_3O_4/NPC on the activation and adsorption/desorption of reactive species through DFT theory. As shown in Fig. 24b, the most stable structure of Co_3O_4/NPC exhibits the cubic configuration of Co_4O_8. It can be found that H_2O is preferentially adsorbed on Co_3O_4 instead of on the NPC carrier. At the same time, weakly adsorbed O_2 is easy to desorb from the loaded Co_3O_4 nanoparticles. As shown in the PDOS of Fig. 24c, it can be found that spin polarization on the surface of the catalyst is stronger. Secondly, most of the Co 3d states are located at the Fermi level and overlap with the N 2p state, which just shows that the unsaturated Co and N atoms have a synergistic effect on the OER process. Generally, the excellent OER catalytic performance is due to the special geometric and electronic effects of Co_3O_4/NPC on the reactive species, as well as activation and adsorption/desorption.

In addition, Huang *et al.*[178] used the (001) surface of CoOOH and single-layer pure graphene of the N-doped graphitic carbon layer for theoretical modeling calculations (Fig. 24d and f). They calculate the standard reaction free energy curve, Δ*G*, through DFT (Fig. 24e), and they find that the rate-determining step on graphene, CoOOH(001), and CoOOH(001)/graphene composites in the OER process is step I. Fig. 24g clearly shows that, due to interfacial interactions, the Bader charges of Co and H on CoOOH/graphene surface are significantly reduced. On the surface of CoOOH, HO* adsorbed H and O lost 0.148e. In contrast, the loss from forming HO* on the CoOOH/graphene surface is only 0.090e, which accelerates the potentially restrictive hydroxylation process, which is beneficial for providing active sites for intermediate adsorption, and ultimately enhances OER activity.

7.3 Doping

Through research, Wang *et al.*[103] found that Fe-doped CoO had a lower band gap and exhibited semiconductor characteristics (Fig. 25a and c). Therefore, Fe doping can increase the conductivity of CoO and further improve the electrocatalytic performance. In addition, it can be found that the state density of the Co 3d orbital after Fe doping with CoO shifts in

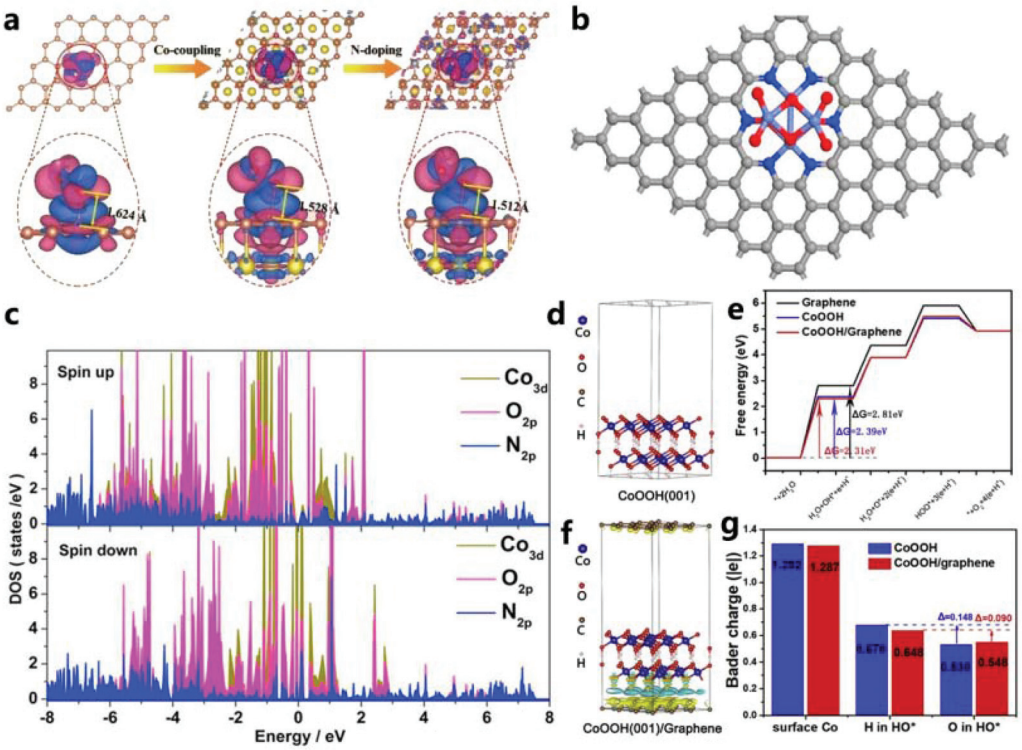

Fig. 24 (a) Redistribution of charge density in C–OOH, Co@C–OOH and Co@N_1C_{31}–OOH systems.[188] Copyright © 2019 Wiley-VCH Verlag GmbH & Co. KGaA, Weinheim. (b) Structure of Co_3O_4/NPC from the top view. (c) Partial density of states of surface Co ions, O atoms and N atoms of NPC in Co_3O_4/NPC.[167] Copyright © 2017 Elsevier B.V. All rights reserved. (d) Side view of the three-dimensional charge density difference graph of CoOOH(001). (e) Gibbs free energy step diagram of the OER on various catalysts. (f) Side view of the three-dimensional charge density difference graph of CoOOH(001)/graphene. (g) Bader charge analysis of the surface Co ions and H or O in the adsorption of HO* on the surface of CoOOH and CoOOH/graphene.[178] Copyright © 2018 Elsevier Ltd. All rights reserved.

the positive direction, which indicates that the doping of Fe increases the energy of the Co atoms and thus makes Co^{3+} transition to a higher valence state (Fig. 25b). Then, by integrating the PDOS distribution map (Fig. 25d), the number of electrons in the Co 3d orbital of Fe-doped CoO is found to be about 7.13, which is 7.25 less than the number of electrons in CoO (theoretical value of Co_2^+ is 7). It can be determined that the lower coordination number of the Co site makes it more capable of adsorbing H_2O, which makes it easier to deprotonate OOH. In addition, the increase in orbital electron density reduces the adsorption energy of OOH* in the OER electrocatalyst. Fe is doped into the CoO orbital, which is conducive to the adsorption of OOH species on the catalyst to promote the OER activity.

Through DFT calculations, Dong *et al.*[189] confirmed that the doping of S optimized the charge environment of the active sites of Co–N and CoO, and promoted the adsorption and desorption of oxygen-containing intermediates, thereby improving the OER performance. By calculating the typical adsorption energy of the four basic steps, Dong *et al.* also studied the free energy diagram of Ce–CoOOH in the OER process (Fig. 25e). To simplify the calculation, they set the OER model to be constructed based on the (001) plane of β-CoOOH (β-CoOOH has the best stability under OER conditions). Through the step diagram, they find that the rate-determining step of OER catalysis is the deprotonation process of HO* to O*, and Ce-doped CoOOH has a lower ΔG and overpotential. In addition, to prove that electrons were transferred from Ce to nearby Co sites, and then to H and HO* (Fig. 25f), the poorer charges of Co and H were also studied. Then, they found that electron transfer between Ce and H weakened the H–O bond, which helped to reduce the energy barrier in the rate-determining step and improve the OER performance.

In short, this section first uses DFT theoretical calculations to determine the electronic structure and catalytic activity of saturated and unsaturated ZIF-67. It also proves that the role of ligands in catalytic activity may be related to the redistribution of charges on active sites due to the change in coordination. In addition, through DFT theoretical calculations, it is confirmed that the sites on ZIF-67 are conducive to metal adsorption, and it is found that the delocalized π electrons in the imidazole group are the most critical for a single atom. They are used as fixed sites, initially forming a strong bond with M ions and keeping them isolated by thermal carbonization. Secondly, the DFT theoretical calculations confirmed the mechanism of Co–C conjugation and N species doping, and revealed that Co_3O_4/NPC and CoOOH/graphene had excellent performances in the OER catalytic reaction.

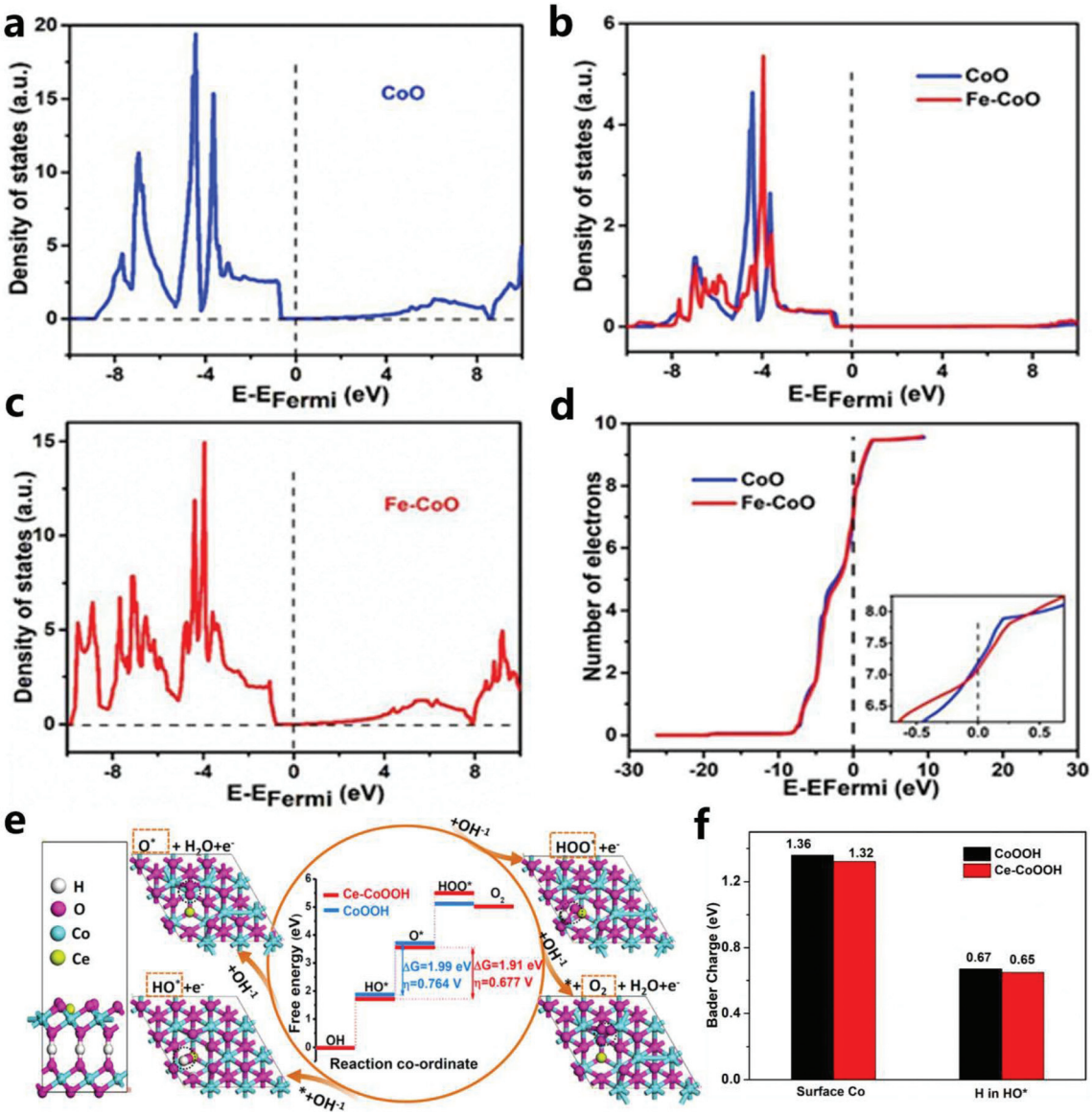

Fig. 25 (a) CoO total density of states. (b) The partial density of the Co 3d orbital state. (c) Fe–CoO total density of states. (d) The number of electrons in the 3d orbital of each Co atom in CoO and Fe–CoO.[103] Copyright © 2018 Elsevier Ltd. All rights reserved. (e) Atomic model and the DFT calculated results for the OER on CoOOH and Ce–CoOOH. (f) Bader charge analysis for surface Co ions and H in HO* adsorption on CoOOH and Ce–CoOOH.[189] Copyright @ 2020, American Chemical Society.

Third, by analyzing the effects of Ce, Fe, and S doping on ZIF-67 derivatives, it can be found that Fe doping is beneficial for the formation of adsorbed OOH species, S doping promotes the adsorption and desorption of oxygen-containing intermediates, and Ce doping not only promotes the adsorption and desorption process of the intermediate, but also weakens the H–O bond, thereby promoting the OER performance.

8 Summary and outlook

Due to inherent poor conductivity of ZIF-67 and its derivatives, other factors need to be considered to improve the design of the composition of the OER catalytic material and the electron transport rate in the structure configuration to enhance the catalytic performance. However, many good properties of nanostructures benefit from the synergy of structural tunability and dopants. Therefore, this review summarizes the OER catalysis of ZIF-67 and its derivatives from the aspects of morphology engineering, composition engineering, doping, and corresponding single-atom catalysis. In addition, the DFT theoretical calculations are summarized to illustrate the mechanism of OER catalysis by ZIF-67 and its derivatives. Through the summary of various aspects, we find that ZIF-67 and its derivatives still have some problems and challenges that cannot be ignored in OER electrocatalysis:

(1) Although there are few studies on the use of ZIF-67-based nanoarrays and single-atom catalysts for OER catalysis, it can be seen that they exhibit good performances at high current densities, which is of great significance to the realization of catalytic industrialization. Therefore, it is necessary to conduct more in-depth research on these catalysts.

(2) In the OER catalysis study based on ZIF-67, no investigations into two-dimensional ZIF-67 were performed. However, two-dimensional catalytic materials exhibit excellent catalytic performance, so research in this field is still necessary.

(3) Research into the doping of ZIF-67 and its derivatives also needs to be perfected, for example, the co-doping of multiple cations or anions and the doping of specific structures.

(4) In terms of ZIF-67 and its derivatives, there is little research on the catalytic mechanism of the OER, and the current mechanism mainly illustrates the discussion based on the Co–N–C active site, which simplifies the actual reaction of the catalyst. Therefore, more in-depth and systematic research is needed, and it is necessary to further improve theoretical guidance for the ZIF-67 system.

Finally, inspired by the directional but flexible structure and inherent advantages of adjustable ZIF-67 components, the exploration of their potential performance and applications will not only be limited to energy storage and conversion but will also lead to long-term developments. With continuous research into the basic science behind complex reaction processes and the accelerated development of characterization and synthesis technology, ZIF-67 and its derivatives will become hot topics for research in the field of catalysis.

Conflicts of interest

The authors declare that they have no known competing financial interests or personal relationships that could have appeared to influence the work reported in this paper.

Acknowledgements

This work was supported by the National Natural Science Foundation of China (Grant No. 51971058 and 52071072), the Fundamental Research Funds for the Central Universities (Grant No. N182312007 and N2023001), the Program for Liaoning Innovative Talents in University (No. LCR2018016), the Liaoning Provincial Natural Science Foundation of China (No. 2019-MS-244), the Liaoning Revitalization Talents Program (No. XLYC1907031), and the Liaoning BaiQianWan Talents Program (No. 2020921082).

References

1 X. Zou and Y. Zhang, *Chem. Soc. Rev.*, 2015, **44**, 5148–5180.
2 Y. Jiao, Y. Zheng, M. Jaroniec and S. Z. Qiao, *Chem. Soc. Rev.*, 2015, **44**, 2060–2086.
3 P. G. Bruce, S. A. Freunberger, L. J. Hardwick and J. M. Tarascon, *Nat. Mater.*, 2012, **11**, 19–29.
4 N. S. Lewis and D. G. Nocera, *Proc. Natl. Acad. Sci. U. S. A.*, 2006, **103**, 15729–15735.
5 B. C. H. Steele and A. Heinzel, *Nature*, 2001, **414**, 345–352.
6 C. C. L. McCrory, S. H. Jung, J. C. Peters and T. F. Jaramillo, *J. Am. Chem. Soc.*, 2013, **135**, 16977–16987.
7 I. C. Man, H. Y. Su, F. Calle-Vallejo, H. A. Hansen, J. I. Martinez, N. G. Inoglu, J. Kitchin, T. F. Jaramillo, J. K. Norskov and J. Rossmeisl, *ChemCatChem*, 2011, **3**, 1159–1165.
8 Z. Y. Ni, H. Wen, S. Q. Zhang, R. Guo, N. Su, X. W. Liu and C. M. Liu, *ChemCatChem*, 2020, **12**, 4962–4999.
9 D. Li, H. Liu and L. Feng, *Energy Fuels*, 2020, **34**, 13491–13522.
10 P. E. M. Siegbahn, *J. Am. Chem. Soc.*, 2009, **131**, 18238–18239.
11 T. A. Betley, Y. Surendranath, M. V. Childress, G. E. Alliger, R. Fu, C. C. Cummins and D. G. Nocera, *Philos. Trans. R. Soc., B*, 2008, **363**, 1293–1303.
12 T. Reier, H. N. Nong, D. Teschner, R. Schlogl and P. Strasser, *Adv. Energy Mater.*, 2017, **7**, 1601275.
13 X. J. Liu, Z. Chang, L. Luo, T. H. Xu, X. D. Lei, J. F. Liu and X. M. Sun, *Chem. Mater.*, 2014, **26**, 1889–1895.
14 C. Xia, Q. Jiang, C. Zhao, M. N. Hedhili and H. N. Alshareef, *Adv. Mater.*, 2016, **28**, 77–85.
15 R. Guo, Y. He, T. Yu, P. Cheng, J. You, H. Lin, C.-T. Chen, T. Chan, X. Liu and Z. Hu, *Chem. Eng. J.*, 2020, 127587.
16 Y. Lee, J. Suntivich, K. J. May, E. E. Perry and Y. Shao-Horn, *J. Phys. Chem. Lett.*, 2012, **3**, 399–404.
17 S. Cherevko, S. Geiger, O. Kasian, N. Kulyk, J. P. Grote, A. Savan, B. R. Shrestha, S. Merzlikin, B. Breitbach, A. Ludwig and K. J. J. Mayrhofer, *Catal. Today*, 2016, **262**, 170–180.
18 G. Wu, K. L. More, C. M. Johnston and P. Zelenay, *Science*, 2011, **332**, 443–447.
19 G. Wu and P. Zelenay, *Acc. Chem. Res.*, 2013, **46**, 1878–1889.
20 S. Zhang, T. Yu, H. Wen, Z. Ni, Y. He, R. Guo, J. You and X. Liu, *Chem. Commun.*, 2020, **56**, 15387–15405.
21 T. Y. Ma, S. Dai, M. Jaroniec and S. Z. Qiao, *J. Am. Chem. Soc.*, 2014, **136**, 13925–13931.
22 J. Suntivich, K. J. May, H. A. Gasteiger, J. B. Goodenough and Y. Shao-Horn, *Science*, 2011, **334**, 1383–1385.
23 M. Gong, Y. G. Li, H. L. Wang, Y. Y. Liang, J. Z. Wu, J. G. Zhou, J. Wang, T. Regier, F. Wei and H. J. Dai, *J. Am. Chem. Soc.*, 2013, **135**, 8452–8455.
24 M. S. Burke, L. J. Enman, A. S. Batchellor, S. H. Zou and S. W. Boettcher, *Chem. Mater.*, 2015, **27**, 7549–7558.
25 J. Quinonero, T. Lana-Villarreal and R. Gomez, *Int. J. Hydrogen Energy*, 2020, **45**, 17076–17087.
26 X. K. Gu, J. C. A. Camayang, S. Samira and E. Nikolla, *J. Catal.*, 2020, **388**, 130–140.
27 S. W. Lee, C. Carlton, M. Risch, Y. Surendranath, S. Chen, S. Furutsuki, A. Yamada, D. G. Nocera and Y. Shao-Horn, *J. Am. Chem. Soc.*, 2012, **134**, 16959–16962.

28 A. Corma, H. Garcia and F. X. Llabrés i Xamena, *Chem. Rev.*, 2010, **110**, 4606–4655.
29 J. Gascon, A. Corma, F. Kapteijn and F. X. Llabrés i Xamena, *ACS Catal.*, 2014, **4**, 361–378.
30 J. Jiang, L. Huang, X. M. Liu and L. H. Ai, *ACS Appl. Mater. Interfaces*, 2017, **9**, 7193–7201.
31 S. Wang and X. Wang, *Small*, 2015, **11**, 3097–3112.
32 S. Wang and X. Wang, *Angew. Chem., Int. Ed.*, 2016, **55**, 2308–2320.
33 J. Ryu, N. Jung, J. H. Jang, H.-J. Kim and S. J. Yoo, *ACS Catal.*, 2015, **5**, 4066–4074.
34 A. Phan, C. J. Doonan, F. J. Uribe-Romo, C. B. Knobler, M. O'Keeffe and O. M. Yaghi, *Acc. Chem. Res.*, 2010, **43**, 58–67.
35 N. L. Torad, M. Hu, S. Ishihara, H. Sukegawa, A. A. Belik, M. Imura, K. Ariga, Y. Sakka and Y. Yamauchi, *Small*, 2014, **10**, 2096–2107.
36 B. You, N. Jiang, M. Sheng, W. S. Drisdell, J. Yano and Y. Sun, *ACS Catal.*, 2015, **5**, 7068–7076.
37 B. You, N. Jiang, M. Sheng, S. Gul, J. Yano and Y. Sun, *Chem. Mater.*, 2015, **27**, 7636–7642.
38 L. Jiao, Y.-X. Zhou and H.-L. Jiang, *Chem. Sci.*, 2016, **7**, 1690–1695.
39 Z. P. Lai, *Curr. Opin. Chem. Eng.*, 2018, **20**, 78–85.
40 X. B. Yang, J. Chen, Y. Q. Q. Chen, P. J. Feng, H. X. Lai, J. T. Li and X. T. Luo, *Nano-Micro Lett.*, 2018, **10**, 15.
41 J. W. Wan, D. Liu, H. Xiao, H. P. Rong, S. Guan, F. Xie, D. S. Wang and Y. D. Li, *ChemComm*, 2020, **56**, 4316–4319.
42 W. Zheng, M. Liu and L. Y. S. Lee, *ACS Catal.*, 2020, **10**, 81–92.
43 H. B. Aiyappa, P. Wilde, T. Quast, J. Masa, C. Andronescu, Y.-T. Chen, M. Muhler, R. A. Fischer and W. Schuhmann, *Angew. Chem., Int. Ed.*, 2019, **58**, 8927–8931.
44 T. Tarnev, H. B. Aiyappa, A. Botz, T. Erichsen, A. Ernst, C. Andronescu and W. Schuhmann, *Angew. Chem., Int. Ed.*, 2019, **58**, 14265–14269.
45 S. Xun, Y. Xu, J. He, D. Jiang, R. Yang, D. Li and M. Chen, *J. Alloys Compd.*, 2019, **806**, 1097–1104.
46 R. Zhu, J. Ding, Y. Xu, J. Yang, Q. Xu and H. Pang, *Small*, 2018, **14**, 1803576.
47 H. Xu, J. Cao, C. Shan, B. Wang, P. Xi, W. Liu and Y. Tang, *Angew. Chem., Int. Ed.*, 2018, **57**, 8654–8658.
48 M. Khalid, A. M. B. Honorato, H. Varela and L. Dai, *Nano Energy*, 2018, **45**, 127–135.
49 Z. Li, Z. Jiang, W. Zhu, C. He, P. Wang, X. Wang, T. Li and L. Tian, *Appl. Surf. Sci.*, 2020, **504**, 144368.
50 W. Wu, J. Liu, G. Chen, Y. Chen and C. Xu, *Int. J. Hydrogen Energy*, 2020, **45**, 1948–1958.
51 Q. Zha, W. Xu, X. Li and Y. Ni, *Dalton Trans.*, 2019, **48**, 12127–12136.
52 X. Guo, G. Liang and A. Gu, *Int. J. Hydrogen Energy*, 2019, **44**, 31020–31028.
53 Y. Wang, Y. Y. Wang, L. Zhang, C. S. Liu and H. Pang, *Inorg. Chem. Front.*, 2019, **6**, 2514–2520.
54 J. Xu, Y. Zhao, M. Li, G. Fan, L. Yang and F. Li, *Electrochim. Acta*, 2019, **307**, 275–284.
55 Y. Wang, M. Zhao, Q. Zhao, Q. Li and H. Pang, *Nanoscale*, 2018, **10**, 15755–15762.
56 D. Dong, Y. Liu and J. Li, *Part. Part. Syst. Charact.*, 2016, **33**, 887–895.
57 L. Li, T. Tian, J. Jiang and L. Ai, *J. Power Sources*, 2015, **294**, 103–111.
58 Q. Shi, S. Fu, C. Zhu, J. Song, D. Du and Y. Lin, *Mater. Horiz.*, 2019, **6**, 684–702.
59 J.-J. Zhou, X. Han, K. Tao, Q. Li, Y.-L. Li, C. Chen and L. Han, *Chem. Eng. J.*, 2018, **354**, 875–884.
60 H. Zhu, J. F. Zhang, R. P. Yanzhang, M. L. Du, Q. F. Wang, G. H. Gao, J. D. Wu, G. M. Wu, M. Zhang, B. Liu, J. M. Yao and X. W. Zhang, *Adv. Mater.*, 2015, **27**, 4752–4759.
61 P. Strasser, *Acc. Chem. Res.*, 2016, **49**, 2658–2668.
62 V. K. Abdelkader-Fernandez, D. M. Fernandes, S. S. Balula, L. Cunha-Silva and C. Freire, *J. Mater. Chem. A*, 2020, **8**, 13509–13521.
63 W. F. Xie, Z. H. Li, M. F. Shao and M. Wei, *Front. Chem. Sci. Eng.*, 2018, **12**, 537–554.
64 J.-F. Qin, J.-Y. Xie, N. Wang, B. Dong, T.-S. Chen, Z.-Y. Lin, Z.-Z. Liu, Y.-N. Zhou, M. Yang and Y.-M. Chai, *J. Colloid Interface Sci.*, 2020, **562**, 279–286.
65 J. Cao, C. Lei, J. Yang, X. Cheng, Z. Li, B. Yang, X. Zhang, L. Lei, Y. Hou and K. Ostrikov, *J. Mater. Chem. A*, 2018, **6**, 18877–18883.
66 S. Li, S. Peng, L. Huang, X. Cui, A. M. Al-Enizi and G. Zheng, *ACS Appl. Mater. Interfaces*, 2016, **8**, 20534–20539.
67 X. Jia, J. Wu, K. Lu, Y. Li, X. Qiao, J. Kaelin, S. Lu, Y. Cheng, X. Wu and W. Qin, *J. Mater. Chem. A*, 2019, **7**, 14302–14308.
68 X. Li, S. You, J. Du, Y. Dai, H. Chen, Z. Cai, N. Ren and J. Zou, *J. Mater. Chem. A*, 2019, **7**, 25853–25864.
69 Y. Wang, Y. Wang, L. Zhang, C.-S. Liu and H. Pang, *Inorg. Chem. Front.*, 2019, **6**, 2514–2520.
70 X. Wang, L. Yu, B. Y. Guan, S. Song and X. W. Lou, *Adv. Mater.*, 2018, **30**, 1801211.
71 V. Ganesan, J. Son and J. Kim, *Nanoscale*, 2021, **13**, 4569–4575.
72 Q. Y. Li, L. Zhang, Y. X. Xu, Q. Li, H. Xue and H. Pang, *ACS Sustainable Chem. Eng.*, 2019, **7**, 5027–5033.
73 D. Ding, K. Shen, X. Chen, H. Chen, J. Chen, T. Fan, R. Wu and Y. Li, *ACS Catal.*, 2018, **8**, 7879–7888.
74 X. Li, Q. Jiang, S. Dou, L. Deng, J. Huo and S. Wang, *J. Mater. Chem. A*, 2016, **4**, 15836–15840.
75 A. Aijaz, J. Masa, C. Roesler, W. Xia, P. Weide, A. J. R. Botz, R. A. Fischer, W. Schuhmann and M. Muhler, *Angew. Chem., Int. Ed.*, 2016, **55**, 4087–4091.
76 D. L. Li, Z. Zong, Z. H. Tang, Z. Liu, S. W. Chen, Y. Tian and X. F. Wang, *ACS Sustainable Chem. Eng.*, 2018, **6**, 5105–5114.
77 J.-G. Li, K. Xie, H. Sun, Z. Li, X. Ao, Z. Chen, K. K. Ostrikov, C. Wang and W. Zhang, *ACS Appl. Mater. Interfaces*, 2019, **11**, 36649–36657.
78 J.-G. Li, Y. Gu, H. Sun, L. Lv, Z. Li, X. Ao, X. Xue, G. Hong and C. Wang, *Nanoscale*, 2019, **11**, 19959–19968.

79 D. Kim, D. Kim, Y. Jeon, Y. Li, J. Lee, J. Kang, L. Y. S. Lee and Y. Piao, *Electrochim. Acta*, 2019, **299**, 213–221.
80 M. Li, C. Bao, Y. Liu, J. Meng, X. Liu, Y. Cai, D. Wuu, Y. Zong, T.-P. Loh and Z. Wang, *RSC Adv.*, 2019, **9**, 16534–16540.
81 V. Jose, A. Jayakumar and J.-M. Lee, *ChemElectroChem*, 2019, **6**, 1485–1491.
82 Y. Pan, K. Sun, S. Liu, X. Cao, K. Wu, W.-C. Cheong, Z. Chen, Y. Wang, Y. Li, Y. Liu, D. Wang, Q. Peng, C. Chen and Y. Li, *J. Am. Chem. Soc.*, 2018, **140**, 2610–2618.
83 J. Li, G. Li, J. Wang, C. Xue, X. Li, S. Wang, B. Han, M. Yang and L. Li, *Inorg. Chem. Front.*, 2020, **7**, 191–197.
84 J. Sun, G. Li, K. Zheng, Y. He, Z. Guo and C. Xu, *Appl. Surf. Sci.*, 2020, **517**, 146183.
85 J. Shi, F. Qiu, W. Yuan, M. Guo and Z.-H. Lu, *Chem. Eng. J.*, 2021, **403**, 126312.
86 Y. Y. Wu, G. D. Li, Y. P. Liu, L. Yang, X. R. Lian, T. Asefa and X. X. Zou, *Adv. Funct. Mater.*, 2016, **26**, 4839–4847.
87 R. Shi, J. Wang, Z. Wang, T. Li and Y.-F. Song, *J. Energy Chem.*, 2019, **33**, 74–80.
88 Y. Li, Z. Wang, J. Hu, S. Li, Y. Du, X. Han and P. Xu, *Adv. Funct. Mater.*, 2020, **30**, 1910498.
89 J. Kim, H. Jin, A. Oh, H. Baik, S. H. Joo and K. Lee, *Nanoscale*, 2017, **9**, 15397–15406.
90 Y. Men, X. Liu, F. Yang, F. Ke, G. Cheng and W. Luo, *Inorg. Chem.*, 2018, **57**, 10649–10655.
91 Q. Liang, Z. Chen, X. Chen and Y. Li, *J. Mater. Chem. A*, 2019, **7**, 20310–20316.
92 J. Li, S. Lu, H. Huang, D. Liu, Z. Zhuang and C. Zhong, *ACS Sustainable Chem. Eng.*, 2018, **6**, 10021–10029.
93 F. Lyu, Y. Bai, Z. Li, W. Xu, Q. Wang, J. Mao, L. Wang, X. Zhang and Y. Yin, *Adv. Funct. Mater.*, 2017, **27**, 1702324.
94 H. J. Fan, M. Knez, R. Scholz, D. Hesse, K. Nielsch, M. Zacharias and U. Gosele, *Nano Lett.*, 2007, **7**, 993–997.
95 J. Park, T. Kwon, J. Kim, H. Jin, H. Y. Kim, B. Kim, S. H. Joo and K. Lee, *Chem. Soc. Rev.*, 2018, **47**, 8173–8202.
96 J.-G. Li, H. Sun, L. Lv, Z. Li, X. Ao, C. Xu, Y. Li and C. Wang, *ACS Appl. Mater. Interfaces*, 2019, **11**, 8106–8114.
97 F. Calle-Vallejo, J. Tymoczko, V. Colic, Q. H. Vu, M. D. Pohl, K. Morgenstern, D. Loffreda, P. Sautet, W. Schuhmann and A. S. Bandarenka, *Science*, 2015, **350**, 185–189.
98 F. Calle-Vallejo, M. D. Pohl, D. Reinisch, D. Loffreda, P. Sautet and A. S. Bandarenka, *Chem. Sci.*, 2017, **8**, 2283–2289.
99 T. Asset, R. Chattot, J. Drnec, P. Bordet, N. Job, F. Maillard and L. Dubau, *ACS Appl. Mater. Interfaces*, 2017, **9**, 25298–25307.
100 T. Asset, N. Job, Y. Busby, A. Crisci, V. Martin, V. Stergiopoulos, C. Bonnaud, A. Serov, P. Atanassov, R. Chattot, L. Dubau and F. Maillard, *ACS Catal.*, 2018, **8**, 893–903.
101 Z. Yu, Y. Bai, S. Zhang, Y. Liu, N. Zhang and K. Sun, *Int. J. Hydrogen Energy*, 2018, **43**, 8815–8823.
102 L. Zhang, T. Mi, M. A. Ziaee, L. Liang and R. Wang, *J. Mater. Chem. A*, 2018, **6**, 1639–1647.
103 X. Ren, F. Lyu, J. Yang, F. Wang, L. Xue, L. Wang, X. Zhang and Q. Wang, *Electrochim. Acta*, 2019, **296**, 418–426.
104 X. Liu, L. Zhou, L. Huang, L. Chen, L. Long, S. Wang, X. Xu, M. Liu, W. Yang and J. Jia, *Electrochim. Acta*, 2019, **318**, 883–891.
105 J. Zhang, F. Li, W. Chen, C. Wang and D. Cai, *Electrochim. Acta*, 2019, **300**, 123–130.
106 H. Chu, D. Zhang, B. Jin and M. Yang, *Appl. Catal., B*, 2019, **255**, 117744.
107 H. Zhang, Z. Yang, X. Wang, S. Yan, T. Zhou, C. Zhang, S. G. Telfer and S. Liu, *Nanoscale*, 2019, **11**, 17384–17395.
108 J. Wu, L. Hu, N. Wang, Y. Li, D. Zhao, L. Li, X. Peng, Z. Cui, L.-J. Ma, Y. Tian and X. Wang, *Appl. Catal., B*, 2019, **254**, 55–65.
109 H. Xu, H. Shang, C. Wang, L. Jin, C. Chen, C. Wang and Y. Du, *Appl. Catal., B*, 2020, **265**, 118605.
110 Y. Li, M. Cui, T. Li, Y. Shen, Z. Si and H.-G. Wang, *Int. J. Hydrogen Energy*, 2020, **45**, 16540–16549.
111 X. Gu, Z. Liu, H. Liu, C. Pei and L. Feng, *Chem. Eng. J.*, 2021, **403**, 126371.
112 Z. Lei, Y. Tan, Z. Zhang, W. Wu, N. Cheng, R. Chen, S. Mu and X. Sun, *Nano Res.*, 2021, **14**, 868–878.
113 J. G. Hou, Y. Z. Wu, B. Zhang, S. Y. Cao, Z. W. Li and L. C. Sun, *Adv. Funct. Mater.*, 2019, **29**, 1808367.
114 R. Guo, A. G. Yan, J. J. Xu, B. T. Xu, T. T. Li, X. W. Liu, T. F. Yi and S. H. Luo, *J. Alloys Compd.*, 2020, **817**, 153246.
115 G. R. Cai, W. Zhang, L. Jiao, S. H. Yu and H. L. Jiang, *Chem*, 2017, **2**, 791–802.
116 F. H. Kong, W. W. Zhang, L. P. Sun, L. H. Huo and H. Zhao, *ChemSusChem*, 2019, **12**, 3592–3601.
117 P. Li, J. Z. Wang, N. Cai, L. Wang, J. Tong and F. Q. Yu, *ChemCatChem*, 2020, **12**, 1639–1646.
118 J. J. Zhou, X. Han, K. Tao, Q. Li, Y. L. Li, C. Chen and L. Han, *Chem. Eng. J.*, 2018, **354**, 875–884.
119 M. Guo, Y. Li, L. Zhou, Q. Zheng, W. Jie, F. Xie, C. Xu and D. Lin, *Electrochim. Acta*, 2019, **298**, 525–532.
120 S. Song, Y. Wang, W. Li, P. Tian, S. Zhou, H. Gao, X. Tian and J. Zang, *J. Alloys Compd.*, 2020, **827**, 154299.
121 S. Wang, X. Yang, Z. Liu, D. Yang and L. Feng, *Nanoscale*, 2020, **12**, 10827–10833.
122 H. Wu, J. Wang, J. Yan, Z. Wu and W. Jin, *Nanoscale*, 2019, **11**, 20144–20150.
123 H. Liu, Z. Liu and L. Feng, *Nanoscale*, 2019, **11**, 16017–16025.
124 Y. Du, G. Cheng and W. Luo, *Nanoscale*, 2017, **9**, 6821–6825.
125 Y. Zhao, S. Xing, X. Meng, J. Zeng, S. Yin, X. Li and Y. Chen, *Nanoscale*, 2019, **11**, 9319–9326.
126 S. Dilpazir, R. Liu, M. Yuan, M. Imran, Z. Liu, Y. Xie, H. Zhao and G. Zhang, *J. Mater. Chem. A*, 2020, **8**, 10865–10874.
127 C.-X. Zhao, B.-Q. Li, M. Zhao, J.-N. Liu, L.-D. Zhao, X. Chen and Q. Zhang, *Energy Environ. Sci.*, 2020, **13**, 1711–1716.

128 X. W. Liu, Z. Y. Ni, Y. He, N. Su, R. Guo, Q. Wang and T. F. Yi, *New J. Chem.*, 2019, **43**, 8711–8721.
129 B. He, X.-C. Wang, L.-X. Xia, Y.-Q. Guo, Y.-W. Tang, Y. Zhao, Q.-L. Hao, T. Yu, H.-K. Liu and Z. Su, *ChemSusChem*, 2020, **13**, 5239–5247.
130 C. Lin, P. Wang, H. Jin, J. Zhao, D. Chen, S. Liu, C. Zhang and S. Mu, *Dalton Trans.*, 2019, **48**, 16555–16561.
131 S. L. Zhang, B. Y. Guan, X. F. Lu, S. Xi, Y. Du and X. W. Lou, *Adv. Mater.*, 2020, **32**, 2002235.
132 K. Xu, Y. Sun, Y. Sun, Y. Zhang, G. Jia, Q. Zhang, L. Gu, S. Li, Y. Li and H. J. Fan, *ACS Energy Lett.*, 2018, **3**, 2750–2756.
133 Y. Sun, K. Xu, Z. Wei, H. Li, T. Zhang, X. Li, W. Cai, J. Ma, H. J. Fan and Y. Li, *Adv. Mater.*, 2018, **30**, 1802121.
134 X. Huang, J. Wang, H. Bao, X. Zhang and Y. Huang, *ACS Appl. Mater. Interfaces*, 2018, **10**, 7180–7190.
135 Y. Tan, Z. Zhang, Z. Lei, W. Wu, W. Zhu, N. Cheng and S. Mu, *J. Power Sources*, 2020, **473**, 228570.
136 F. Tang, X. Gao and Z. Jin, *Electrochim. Acta*, 2020, **337**, 135807.
137 W.-H. Lai, L.-F. Zhang, W.-B. Hua, S. Indris, Z.-C. Yan, Z. Hu, B. Zhang, Y. Liu, L. Wang, M. Liu, R. Liu, Y.-X. Wang, J.-Z. Wang, Z. Hu, H.-K. Liu, S.-L. Chou and S.-X. Dou, *Angew. Chem., Int. Ed.*, 2019, **58**, 11868–11873.
138 L. Tao, C.-Y. Lin, S. Dou, S. Feng, D. Chen, D. Liu, J. Huo, Z. Xia and S. Wang, *Nano Energy*, 2017, **41**, 417–425.
139 S. Dilpazir, H. He, Z. Li, M. Wang, P. Lu, R. Liu, Z. Xie, D. Gao and G. Zhang, *ACS Appl. Energy Mater.*, 2018, **1**, 3283–3291.
140 X. Sun, S. Sun, S. Gu, Z. Liang, J. Zhang, Y. Yang, Z. Deng, P. Wei, J. Peng, Y. Xu, C. Fang, Q. Li, J. Han, Z. Jiang and Y. Huang, *Nano Energy*, 2019, **61**, 245–250.
141 Y. Y. Liang, Y. G. Li, H. L. Wang, J. G. Zhou, J. Wang, T. Regier and H. J. Dai, *Nat. Mater.*, 2011, **10**, 780–786.
142 H. Li, Y. He, T. He, S. Yan, X. Ma and J. Chen, *J. Mater. Sci.: Mater. Electron.*, 2019, **30**, 21388–21397.
143 L. Han, S. J. Dong and E. K. Wang, *Adv. Mater.*, 2016, **28**, 9266–9291.
144 Q. L. Zhu and Q. Xu, *Chem. Soc. Rev.*, 2014, **43**, 5468–5512.
145 N. Stock and S. Biswas, *Chem. Rev.*, 2012, **112**, 933–969.
146 T. Meng, J. Qin, S. Wang, D. Zhao, B. Mao and M. Cao, *J. Mater. Chem. A*, 2017, **5**, 7001–7014.
147 E. Zhang, Y. Xie, S. Ci, J. Jia, P. Cai, L. Yi and Z. Wen, *J. Mater. Chem. A*, 2016, **4**, 17288–17298.
148 X. Yang, J. Chen, Y. Chen, P. Feng, H. Lai, J. Li and X. Luo, *Nano-Micro Lett.*, 2018, **10**, 15.
149 H. Zhou, M. Zheng, H. Tang, B. Xu, Y. Tang and H. Pang, *Small*, 2020, **16**, e1904252.
150 W. Xu, W. Xie and Y. Wang, *ACS Appl. Mater. Interfaces*, 2017, **9**, 28642–28649.
151 X. Yan, L. Tian, S. Atkins, Y. Liu, J. Murowchick and X. Chen, *ACS Sustainable Chem. Eng.*, 2016, **4**, 3743–3749.
152 K. Jin, J. Park, J. Lee, K. D. Yang, G. K. Pradhan, U. Sim, D. Jeong, H. L. Jang, S. Park, D. Kim, N.-E. Sung, S. H. Kim, S. Han and K. T. Nam, *J. Am. Chem. Soc.*, 2014, **136**, 7435–7443.
153 H. Kim, J. Park, I. Park, K. Jin, S. E. Jerng, S. H. Kim, K. T. Nam and K. Kang, *Nat. Commun.*, 2015, **6**, 8253.
154 J. Wang, C. Chen, N. Cai, M. Wang, H. Li and F. Yu, *Nanoscale*, 2021, **13**, 1354–1363.
155 J. Li, G. Du, X. Cheng, P. Feng and X. Luo, *Chin. J. Catal.*, 2018, **39**, 982–987.
156 T. Liu, F. Yang, G. Cheng and W. Luo, *Small*, 2018, **14**, 1703748.
157 Y. Guo, J. Tang, Z. Wang, Y.-M. Kang, Y. Bando and Y. Yamauchi, *Nano Energy*, 2018, **47**, 494–502.
158 L.-L. Wu, Q.-S. Wang, J. Li, Y. Long, Y. Liu, S.-Y. Song and H.-J. Zhang, *Small*, 2018, **14**, 1704035.
159 S. Liu, X. Zhang, G. Wang, Y. Zhang and H. Zhang, *ACS Appl. Mater. Interfaces*, 2017, **9**, 34269–34278.
160 Y. Guo, J. Tang, H. Qian, Z. Wang and Y. Yamauchi, *Chem. Mater.*, 2017, **29**, 5566–5573.
161 S. Anantharaj, S. R. Ede, K. Sakthikumar, K. Karthick, S. Mishra and S. Kundu, *ACS Catal.*, 2016, **6**, 8069–8097.
162 Y. Zheng, L. Zhang, H. Huang, F. Wang, L. Yin, H. Jiang, D. Wang, J. Yang and G. Zuo, *Int. J. Hydrogen Energy*, 2019, **44**, 27465–27471.
163 D. H. He, X. L. Wu, W. Liu, C. J. Lei, C. L. Yu, G. K. Zheng, J. J. Pan, L. C. Lei and X. W. Zhang, *Chin. Chem. Lett.*, 2019, **30**, 229–233.
164 K. Ao, J. Dong, C. Fan, D. Wang, Y. Cai, D. Li, F. Huang and Q. Wei, *ACS Sustainable Chem. Eng.*, 2018, **6**, 10952–10959.
165 X. Wang, X. Huang, W. Gao, Y. Tang, P. Jiang, K. Lan, R. Yang, B. Wang and R. Li, *J. Mater. Chem. A*, 2018, **6**, 3684–3691.
166 M. Yang, W. Lu, R. Jin, X.-C. Liu, S. Song and Y. Xing, *ACS Sustainable Chem. Eng.*, 2019, **7**, 12214–12221.
167 G.-l. Zhuang, Y.-f. Gao, X. Zhou, X.-y. Tao, J.-m. Luo, Y.-j. Gao, Y.-l. Yan, P.-y. Gao, X. Zhong and J.-g. Wang, *Chem. Eng. J.*, 2017, **330**, 1255–1264.
168 S. Liu, X. W. Chen, S. Wang, Z. Yang, J. X. Gao, P. Zhu, X. S. Zhao and G. X. Wang, *Electrochim. Acta*, 2018, **292**, 707–717.
169 P. Li, J. Wang, N. Cai, L. Wang, J. Tong and F. Yu, *ChemCatChem*, 2020, **12**, 1639–1646.
170 J. M. Zhou, H. Y. Zheng, Q. J. Luan, X. B. Huang, Y. Li, Z. S. Xi, G. L. Lu, L. W. Xing and Y. Q. Li, *Sustainable Energy Fuels*, 2019, **3**, 3201–3207.
171 L. Xu, X. Wang, L. Chai, T.-T. Li, Y. Hu, J. Qian and S. Huang, *Mater. Lett.*, 2019, **248**, 181–184.
172 X. Wen, X. Yang, M. Li, L. Bai and J. Guan, *Electrochim. Acta*, 2019, **296**, 830–841.
173 Y. Li, H. Xu, H. Huang, C. Wang, L. Gao and T. Ma, *ChemComm*, 2018, **54**, 2739–2742.
174 Y. Hao, Y. Xu, J. Liu and X. Sun, *J. Mater. Chem. A*, 2017, **5**, 5594–5600.
175 P. He, X. Y. Yu and X. W. Lou, *Angew. Chem., Int. Ed.*, 2017, **56**, 3897–3900.
176 C. Wang, W. Chen, D. Yuan, S. Qian, D. Cai, J. Jiang and S. Zhang, *Nano Energy*, 2020, **69**, 104453.

177 Y. Zhao, G. Fan, L. Yang, Y. Lin and F. Li, *Nanoscale*, 2018, **10**, 13555–13564.
178 X. Wang, Z. Ma, L. Chai, L. Xu, Z. Zhu, Y. Hu, J. Qian and S. Huang, *Carbon*, 2019, **141**, 643–651.
179 X. Liu, J. Dong, B. You and Y. Sun, *RSC Adv.*, 2016, **6**, 73336–73342.
180 L. L. Chai, Z. Y. Hu, X. Wang, Y. W. Xu, L. J. Zhang, T. T. Li, Y. Hu, J. J. Qian and S. M. Huang, *Adv. Sci.*, 2020, **7**, 1903195.
181 L. Feng, R. Ding, Y. Chen, J. Wang and L. Xu, *J. Power Sources*, 2020, **452**, 227837.
182 W. Chen, Y. Zhang, G. Chen, Y. Zhou, X. Xiang and K. K. Ostrikov, *ACS Sustainable Chem. Eng.*, 2019, **7**, 8255–8264.
183 C. Wu, Y. Du, Y. Fu, D. Feng, H. Li, Z. Xiao, Y. Liu, Y. Yang and L. Wang, *Sustainable Energy Fuels*, 2020, **4**, 1654–1664.
184 Y. Zhang, Y. Qiu, X. Ji, T. Ma, Z. Ma and P. A. Hu, *ChemSusChem*, 2019, **12**, 3792–3800.
185 C. Sun, Q. Dong, J. Yang, Z. Dai, J. Lin, P. Chen, W. Huang and X. Dong, *Nano Res.*, 2016, **9**, 2234–2243.
186 Z. Ni, H. Liang, Z. Yi, R. Guo, C. Liu, Y. Liu, H. Sun and X. Liu, *Coord. Chem. Rev.*, 2021, **441**, 213983.
187 Z. Li, X. Zhang, Y. Kang, C. C. Yu, Y. Wen, M. Hu, D. Meng, W. Song and Y. Yang, *Adv. Sci.*, 2020, **8**, 2002631.
188 Z. Chen, Y. Ha, H. Jia, X. Yan, M. Chen, M. Liu and R. Wu, *Adv. Energy Mater.*, 2019, **9**, 1803918.
189 J. Li, S. Zou, X. Liu, Y. Lu and D. Dong, *ACS Sustainable Chem. Eng.*, 2020, **8**, 10009–10016.